Thesis for *Doctor of Philosophy*

Hydrogen Desorption in Steels

Song, Eun Ju (Song, Eun Ju)

Computational Metallurgy

Graduate Institute of Ferrous Technology

Pohang University of Science and Technology

2015

Contents

List of Figures

Chapter 1

Introduction

Hydrogen embrittlement can be defined collectively as phenomena that lead to mechanical degradation, in particular a loss of ductility and toughness in materials containing hydrogen. It has been a subject of significant research since the first report in 1874 (Johnson, 1874). It is one of the important issues in the engineering industries because its susceptibility to hydrogen increases with the strength of steel (Hirth, 1980). In addition, it may become a challenging issue in the storage and transportation of hydrogen in the so-called "hydrogen economy" (Rhodes *et al.*, 2007).

The governing mechanism or mechanisms for hydrogen embrittlement lack clarity because they then not to be quantitative and in general do not have direct links with fracture. However, it is generally accepted that hydrogen embrittlement involves interaction with hydrogen and defects sites and hence requires the hydrogen to be in a diffusible form (Beachem, 1972; Nagumo, 2004; Troiano, 1960). It is established that the passage of hydrogen is hindered by lattice imperfections which tend to attract and bind it; this phenomenon is known as trapping (Darken & Smith, 1949). It is difficult to observe a hydrogen atom in steel due to its small volume and light weight. Only few studies have reported the direct observations of hydrogen (deuterium) (Takahashi *et al.*, 2010, 2012). Traps can be

useful in pinning down the hydrogen atoms, thereby preventing them from diffusing to stress concentrations to participate in damage.

One of the experimental techniques to investigate the trapping is thermal desorption spectroscopy (TDS) which monitors the rate at which hydrogen is released from a sample during continuous heating. However, it is indirect so the resulting data of the curve require interpretation. There are some methods to interpret the TDS results (Choo & Lee, 1982; Kissinger, 1957; McNabb & Foster, 1963; Oriani, 1970) but, they have limitations to be applied to samples with different kinds of traps or to samples which matrix phase is not a single phase. In this study, a new numerical model is suggested and by using this model, hydrogen desorption in complex steels is investigated.

References

Beachem, C. (1972). A new model for hydrogen-assisted cracking (hydrogen embrittlement). *Metallurgical Transactions*, **3**, 441–455. 1

Choo, W. & Lee, J.Y. (1982). Thermal analysis of trapped hydrogen in pure iron. *Metallurgical Transactions A*, **13**, 135–140. 2

Darken, L.S. & Smith, R.P. (1949). Behavior of hydrogen in steel during and after immersion in acid. *Corrosion*, **5**, 1–16. 1

Hirth, J.P. (1980). Effects of hydrogen on the properties of iron and steel. *Metallurgical Transactions A*, **11**, 861–890. 1

Johnson, W.H. (1874). On some remarkable changes produced in iron and steel by the action of hydrogen and acids. *Proceedings of the Royal Society of London*, **23**, 168–179. 1

Kissinger, H.E. (1957). Reaction kinetics in differential thermal analysis. *Analytical Chemistry*, **29**, 1702–1706. 2

McNabb, A. & Foster, P. (1963). A new analysis of the diffusion of hydrogen in iron and ferritic steels. *Trans. AIME*, **227**, 618. 2

Nagumo, M. (2004). Hydrogen related failure of steels–a new aspect. *Materials Science and Technology*, **20**, 940–950. 1

Oriani, R.A. (1970). The diffusion and trapping of hydrogen in steel. *Acta Metallurgica*, **18**, 147–157. 2

Rhodes, P., Skogsberg, L. & Tuttle, R. (2007). Pushing the limits of metals in corrosive oil and gas well environments. *Corrosion*, **63**, 63–100. 1

Takahashi, J., Kawakami, K., Kobayashi, Y. & Tarui, T. (2010). The first direct observation of hydrogen trapping sites in TiC precipitation-hardening steel through atom probe tomography. *Scripta Materialia*, **63**, 261–264. 1

Takahashi, J., Kawakami, K. & Tarui, T. (2012). Direct observation of hydrogen-trapping sites in vanadium carbide precipitation steel by atom probe tomography. *Scripta Materialia*, **67**, 213–216. 1

Troiano, A.R. (1960). The role of hydrogen and other interstitials in the mechanical behavior of metals. *Trans. ASM*, **52**, 54–80. 1

Chapter 2

Literature Review

The aim of this work is to analyze the thermal desorption of hydrogen in variety of steels so related topics are reviewed in this chapter. The theories for hydrogen embrittlement are introduced briefly, although the focus remains on the studies about hydrogen trapping.

2.1 Hydrogen Embrittlement

Hydrogen embrittlement can be defined collectively as phenomena that lead to mechanical degradation, in particular a loss of ductility and toughness in materials containing hydrogen. The effect has been observed in many materials such as Ti, Nb, V, and Al (Bastien & Azou, 1951; Dayal & Parvathavarthini, 2003) and is particularly serious in strong steels (Hirth, 1980; Louthan Jr *et al.*, 1972).

Recently, much research using atomistic simulation has been carried out to reveal aspects of the mechanisms (Ko *et al.*, 2012; Song & Curtin, 2013; Taketomi *et al.*, 2008; Wen *et al.*, 2003). However, the confidence in the underlying mechanisms is lacking even though the original discovery was quite some time ago in on 1874 (Johnson, 1874). The proposed mechanisms are internal pressure (Tetelman & Robertson, 1961; Zapffe

4

& Sims, 1941), hydride formation (Gahr *et al.*, 1977), hydrogen enhanced decohesion (HEDE) (Oriani & Josephic, 1974; Troiano, 1960), hydrogen enhanced local plasticity (HELP) (Beachem, 1972; Birnbaum & Sofronis, 1994; Robertson, 2001) and and hydrogen-enhanced strain-induced vacancy (HESIV) (Nagumo, 2004) mechanisms. Hydride formation mechanism is relatively well-established for hydride forming metals for example, Nb (Gahr *et al.*, 1977). However, hydride formation mechanism is not proper for iron and steel since no hydride is stable up to hydrogen pressure of $2\,\mathrm{GPa}$ (Louthan Jr *et al.*, 1972).

In the internal pressure theory, the atomic hydrogen is absorbed and accumulated at internal defects such as voids (Zapffe & Sims, 1941). Then it forms molecular hydrogen or reacts with the carbon in matrix and forms methane. This results in a very high internal pressure that scales inversely with the size of the gas bubble and assists the growth of voids or cracks. This mechanism can be supported by blister formation without external stress (Rogers, 1968). The high pressure developed by formation of molecular hydrogen enhances void growth and crack propagation. Blister formation has been reported in some literature (Pérez Escobar *et al.*, 2011; Rogers, 1968). An example is shown in Fig. 2.1. However, it has been considered not to be general one because of the observation of the crack growth at sub-atmospheric hydrogen pressures (Hancock & Johnson, 1966).

The absorbed hydrogen may reduce the cohesive energy of the iron in lattice, thereby making it easier to cleave the metal (Oriani & Josephic, 1974; Troiano, 1960). In other words, it can be considered that hydrogen reduces the energy of the surface created in crack growth (Petch & Stables, 1952). This concept is supported by the good correlation between the tolerance for cleavage fracture and hydrogen concentration (Gerberich *et al.*, 1996) and the crack tip angle decrease with increasing H_2 pressure when the crack plane is parallel to $\{100\}_\alpha$ (Vehoff & Rothe, 1983).

Recently, a molecular dynamics study revealed a 10% reduction in
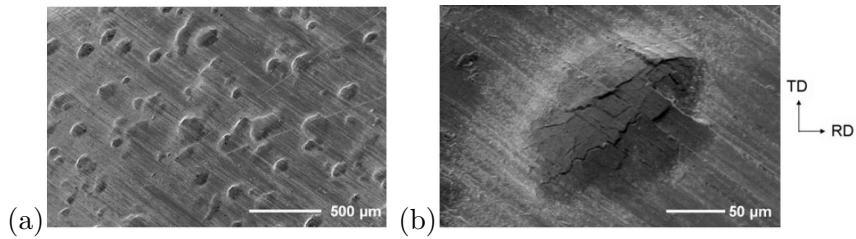
Figure 2.1: Blister formation in pure iron. Hydrogen was charged for 1 h at a current density of $500\,\mathrm{A\,m^{-2}}$ with arsenic-poisoned electrolyte (Pérez Escobar *et al.*, 2011).
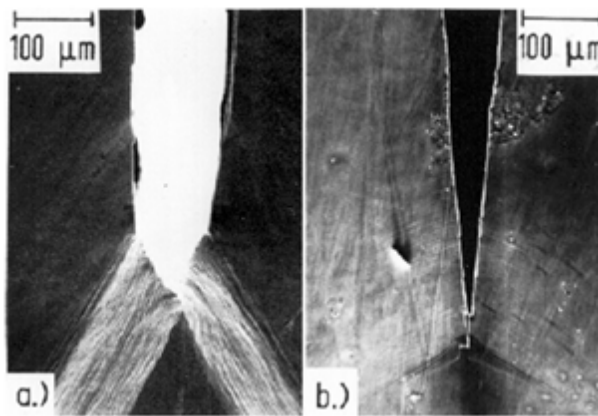
Figure 2.2: $\{100\}_\alpha$ crack tip of Fe-3Si wt% single crystals after straining in (a) vacuum and (b) hydrogen. (Vehoff & Rothe, 1983)

shear modulus by 1 at.% hydrogen dissolved in iron (Taketomi *et al.*, 2008). It was also found that the hydrogen reduced the shear modulus by in situ electrochemical nanoindentation (ECNI) technique in various metals (Barnoush & Vehoff, 2008, 2010; Barnoush *et al.*, 2010); however, it was also mentioned that the reported reduction in the bond strength is not enough to explain the hydrogen embrittlement (Barnoush & Vehoff, 2010).

A more recent mechanism used to explain the effect of hydrogen is hydrogen-enhanced local plasticity (HELP) model (Beachem, 1972; Birnbaum & Sofronis, 1994; Robertson, 2001). It is based on the stress shielding effect to increase the mobility of dislocations. Hydrogen forms Cottrell atmospheres (Cottrell & Jaswon, 1949) around dislocation cores. Accordingly, it reduces the strain field of individual dislocations, thus the interaction between dislocations is reduced, so the mobility of dislocations increases in a way that localises plasticity, leading to fracture that is brittle as a macroscopic scale. The shielding effect is supported by transmission electron microscopy (TEM) observations of enhanced dislocation motion (Sofronis & Robertson, 2002), fracture surfaces showing high local plastic-like deformation and slip bands at crack tips (Abraham & Altstetter, 1995) and reduced dislocation-dislocation separations in dislocation pile-ups at dislocation barriers (Ferreira *et al.*, 1998). However, the thin specimens used for TEM are under plane-strain conditions, so a direct connection with real situations is difficult. Moreover, to make this mechanism to be effective, the dislocation should move with hydrogen (Myers *et al.*, 1992). Thus, it can be applied only when the strain rate is slower than the ability of hydrogen to diffuse with dislocations.

2.2 Hydrogen Trapping

2.2.1 Thermal Desorption Analysis

Hydrogen can be absorbed during the process such as welding, electroplating, cathodic protection and pickling or it can be absorbed during use. Even though the solubility of hydrogen in metal is very small, for example, the solubility of hydrogen in pure iron in equilibrium with 1 atm of H_2 is 0.0001 ppmw (San-Martin & Manchester, 1990) at room temperature, however, much larger amounts of hydrogen can be absorbed into metal due to the trapping effect of defects such as dislocations, grain boundaries and vacancies (Darken & Smith, 1949). The main effects of trapping are to increase the hydrogen solubility and to decrease the apparent diffusivity.
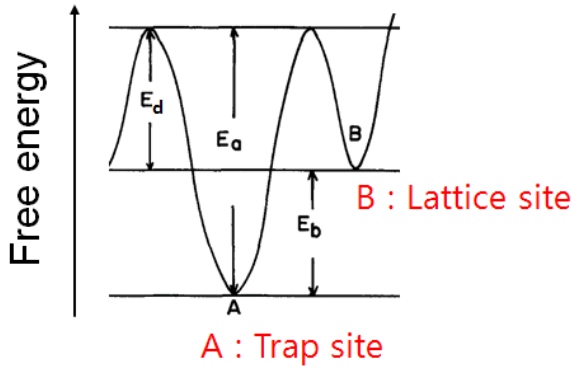
Figure 2.3: The energy level of hydrogen around trap sites.

A property of trapped hydrogen is characterised by a binding energy E_b and trap number density N_t. Fig. 2.3 shows the energy level of hydrogen around trap sites. E_d is the diffusion activation energy, and E_a is the detrapping activation energy. Several methods to evaluate hydrogen trapping have been developed such as thermal desorption analysis (TDA) and permeation techniques. In this study, TDA was used as a

8

main method and a method to assess TDA results was investigated.
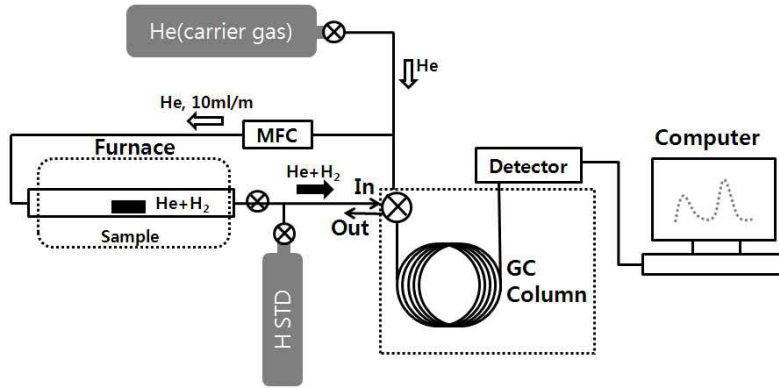
Figure 2.4: Schematic illustration of the typical set-up for thermal desorption analysis with gas chromatography (Ryu, 2012).

TDA is used to measure the hydrogen desorption rate as the sample containing hydrogen is heated at the constant rate. It gives information about the binding energies of traps such as dislocations or grain boundaries in steels. In general, stronger traps release hydrogen at higher temperatures in a TDA experiments. Fig. 2.4 shows a schematic illustration of the TDA equipment with gas chromatography. The specimen is charged prior to TDA, and then it is located in a furnace. As the temperature increases with the given rate, the trapped hydrogen is able to escape from the trap sites and diffuses out. With He as a carrier gas, the gas including desorbed hydrogen flows to the gas chromatograph. Since the gas is separated according to its molecular weight, the amount of hydrogen can be obtained. In this study, a standard gas mixture of He + H_2 was used to calibrate the chromatograph.

There are several methods to evaluate TDA results and they can be categorized as three models, Kissinger model (Choo & Lee, 1982; Kissinger, 1957), McNabb-Foster model (McNabb & Foster, 1963) and Oriani model (Oriani, 1970). The summarized hydrogen trap binding en-

ergies obtained from literature are listed in Table 2.1. It shows a large difference in interpretation depending on the method. For example, the binding energy for grain boundary varies from 10 to $59\,\mathrm{kJ\,mol^{-1}}$ (Asaoka *et al.*, 1977; Choo & Lee, 1982; Ono & Meshii, 1992). Thus, the values cannot be used practically. Also, the prediction of hydrogen desorption profile as a function of temperature with practically meaningful parameters is difficult. The method to assess TDA results remains to be improved.

Moreover, the Kissinger model is not applicable to austenite since it ignores the diffusion which has significant effects in the case of hydrogen in austenite. There are some studies which investigated the trap binding energies in austenite using the Kissinger model (Ningshen *et al.*, 2001; Park *et al.*, 2002; So *et al.*, 2009). However, the detrapping activation energies are less than the diffusion activation energy $48\text{-}54\,\mathrm{kJ\,mol^{-1}}$(Xiukui *et al.*, 1989). For example, the reported detrapping activation energy is $26\,\mathrm{kJ\,mol^{-1}}$ for dislocations (Park *et al.*, 2002).

2.2.2   Theories for Hydrogen Trapping

A reaction rate theory by Kissinger (1957) was first applied to analyze the H desorption by Choo & Lee (1982). It determines the detrapping activation energy from the peak temperature T_p. The desorption rate is described as

$$\frac{dX}{dt} = A(1 - X)\exp\left(\frac{-E_a}{RT}\right) \tag{2.1}$$

where X is the fraction of hydrogen released, A is an empirical constant, E_a is the detrapping activation energy, R is the gas constant, and T is the absolute temperature. When a constant heating rate ϕ is used, the maximum desorption rate can be obtained when the derivative of equation 2.1 is zero. Thus we can obtain E_a from

$$\frac{\partial \ln\left(\phi/T_p^2\right)}{\partial\left(1/T_p\right)} = \frac{-E_a}{R} \tag{2.2}$$

Table 2.1: Some trap binding energies $(\mathrm{kJ\,mol^{-1}})$ in ferritic steels from the literature. The value in bracket indicates activation energy to escape from the trap.

trapping sites	binding energy	reference
grain boundary	(17)	Choo & Lee (1982)
grain boundary	45, 47	Ono & Meshii (1992)
grain boundary	59	Asaoka *et al.* (1977)
grain boundary, dislocation	(22)	Wei *et al.* (2004)
dislocation	25	Oriani (1970)
dislocation	36	Hill & Johnson (1959)
dislocation	59	Kumnick & Johnson (1980)
dislocation	(27)	Choo & Lee (1982)
surface	71	Chornet & Coughlin (1972)
Fe oxide interface	(51,70)	Lee *et al.* (1984)
AlN interface	65	Podgurski & Oriani (1972)
MnS interface	(72)	Lee & Lee (1983)
Al_2O_3 interface	(79)	Lee & Lee (1986)
substitutional Ti	(22)	Pressouyre & Bernstein (1978)
TiC interface	(95)	Pressouyre & Bernstein (1978)
TiC interface	(86)	Wei *et al.* (2004)
TiC interface	(87)	Lee & Lee (1984)
TiC interface (semihorent)	(50)	Wei *et al.* (2004)
NbC interface	(63-68)	Wallaert *et al.* (2014)
NbN interface	(100-143)	Wallaert *et al.* (2014)

Much research has been carried out with this model, for example, Choo & Lee (1982); Lee & Lee (1984); Takai & Watanuki (2003); Wei *et al.* (2004). If there are results with different heating rates, the binding energy can be obtained simply from equation 2.2. However, the trap density which affects the peak temperature is not considered in equation 2.2. Moreover, the model deals with homogeneous reactions (for example, a color change in a chemical reaction), whereas the experiments involve the diffusion of H toward the surface. It is possible that the rate determining step is diffusion not the detrapping, especially when diffusivity of H is low enough or sample thickness is relatively large. Thus it cannot explain the different results from varying sample thicknesses or multiple traps.

A second model is suggested by McNabb & Foster (1963). It is the most general model dealing with H in both the lattice and traps. They considered the kinetics of trapping and detrapping with the activation energy law and mass conservation.

$$\frac{d\theta_t}{dt} = k\theta_l(1 - \theta_t) - p\theta_t \tag{2.3}$$

θ_l, θ_t are the occupancies of H in lattice and trap sites, defined as the concentration divided by the trap density, N_t is the trap density, C_l and C_t are hydrogen concentrations in lattice and trap, respectively, and k, p represent the rates of hydrogen trapping and escaping, respectively. k and p can be described by

$$
\begin{aligned}
k &= k_0 \exp\left(\frac{-E_d}{RT}\right), \\
p &= p_0 \exp\left(\frac{-(E_d + E_b)}{RT}\right)
\end{aligned}
\tag{2.4}
$$

Here, k_0 and p_0 are pre exponential factors, E_d is the diffusion activation energy, and E_b is the trap binding energy. This model was used in some studies to analyze the permeation test results (Kumnick & Johnson, 1980;

Robertson & Thompson, 1980). It has been also used to predict TDA results (Ebihara *et al.*, 2007, 2009; Enomoto *et al.*, 2006; Turnbull *et al.*, 1997). However due to the too many fitting parameters, k_0, p_0, E_b, N_t, those researches focused on the modeling itself and could not give proper values for the binding energy or trap density.

The final model is suggested by Oriani (1970). Hydrogen diffusion can be expressed as

$$\frac{dC_l}{dt} + \frac{dC_t}{dt} = D_l \frac{d^2 C_l}{dx^2} \tag{2.5}$$

where D_l is the H diffusivity in the lattice. It is assumed that local equilibrium is established between the H in the trap and lattice. Then

$$
\begin{aligned}
\mu_l &= \mu_l^0 - RT \ln \frac{\theta_l}{1 - \theta_l} \\
&= \mu_t^0 - RT \ln \frac{\theta_t}{1 - \theta_t} = \mu_t
\end{aligned}
\tag{2.6}
$$

where μ_l, μ_t are chemical potential of H in lattice, trap and μ_l^0, μ_t^0 are their reference state values. If we assume $\theta_l \ll 1$, which is reasonable since hydrogen solubility is very low, then

$$\frac{\theta_t}{\theta_l(1 - \theta_t)} = \exp\left(\frac{\mu_l^0 - \mu_t^0}{RT}\right) = \exp\left(\frac{E_b}{RT}\right) \tag{2.7}$$

It should be noted that equation 2.7 can be obtained from the McNabb-Foster model also. With the local equilibrium assumption, equation 2.3 should be zero. If the pre exponential factor k_0 and p_0 are same, equation 2.7 can be obtained from equation 2.3.

From equation 2.7, C_t can be obtained as equation 2.8.

$$C_t = \frac{N_t C_l \exp\left(E_b/RT\right)}{N_l + C_l \exp\left(E_b/RT\right)} \tag{2.8}$$

With the assumption $\theta_t \ll 1$, C_t can be obtained in a more simple form

from equation 2.7.

$$C_t = \frac{N_t}{N_l} \exp\left(E_b/RT\right) \tag{2.9}$$

Thus equation 2.5 can be written as

$$\frac{dC_l}{dt} = D_{app} \frac{d^2 C_l}{dx^2} \tag{2.10}$$

where the apparent diffusivity D_{app} is

$$D_{app} = \frac{D_l}{1 + \frac{N_t}{N_l} \exp\left(E_b/RT\right)} \tag{2.11}$$

This model is used widely to analyze the effective diffusivity from permeation tests to obtain trap density and binding energy. However, through the effective diffusivity only a single trap can be analyzed and cannot explain different binding energies from different traps. Also, the assumption $\theta_t \ll 1$ is not relevant especially when dealing with TDA results. For example, when the binding energy is $50\,\mathrm{kJ\,mol^{-1}}$, the trap occupancy is almost 1 with $C_l = 0.001\,\mathrm{ppmw}$ at T $= 300\,\mathrm{K}$. The trap occupancy for ferrite with traps which have binding energies 15, 38, $50\,\mathrm{kJ\,mol^{-1}}$ as a function of the lattice H concentration is shown in Fig. 2.5. The results were calculated by the equation 2.7.

Without using the assumption $\theta_t \ll 1$,

$$\frac{dC_t}{dC_l} = \frac{N_t N_l \exp\left(E_b/RT\right)}{\{N_l - C_l + C_l \exp\left(E_b/RT\right)\}^2} \tag{2.12}$$

D_{app} can be obtained as

$$D_{app} = \frac{D_l}{1 + \frac{N_t N_l \exp\left(E_b/RT\right)}{\{N_l - C_l + C_l \exp\left(E_b/RT\right)\}^2}} \tag{2.13}$$

However, equation 2.13 is too complex to be used in practice because of the term C_l which varies with time and position.
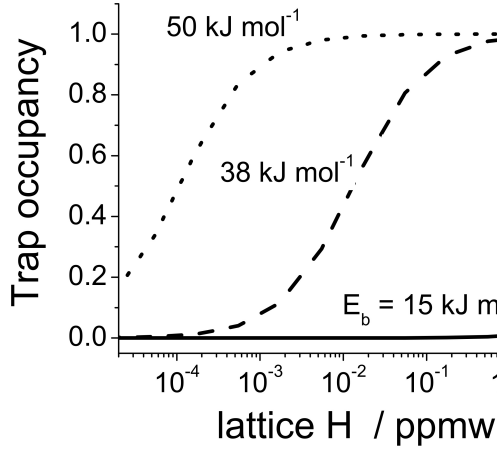
Figure 2.5: The trap occupancy as a function of lattice concentration.

It is also possible to obtain the binding energy from equation 2.8. From the experimentally measured hydrogen concentration, the trapped hydrogen was obtained if the lattice hydrogen concentration is known. By changing the charging temperature, the trapped hydrogen concentration as a function of time can be obtained and from those values, the binding energy and trap density can be found. However, the lattice hydrogen concentration is not clear especially when hydrogen is charged electrochemically. Also, due to the time gap between charging and measuring, it is difficult to obtain the exact amount of hydrogen.

Research using the apparent diffusivity to predict TDA results has been reported (Yamaguchi & Nagumo, 2003). They used the effective diffusivity with the solution of Fick's law but did not obtain enough consistency. That might be caused from the $\theta_t \ll 1$ assumption. Also, the solution was ideal for constant temperature, *i.e.*, constant diffusivity which is not proper for TDA prediction which involves continuous heating.

Recently, equation 2.1 from Kissinger method was linked with diffusion (Wei *et al.*, 2012). For example, equation 2.14 holds for the simple

15

case of plate specimen of initially uniform hydrogen distribution and one-dimensional diffusion.

$$\frac{dX}{dt} = \frac{\pi^2 D}{4d^2}(1 - X) \tag{2.14}$$

In this equation, d is the half-thickness of the sample and D is the diffusivity which can be expressed as $D = D_0 \exp\left(\frac{-E_d}{RT}\right)$. The authors used D as an apparent diffusivity which includes the effects of trapping and related equation 2.14 with equation 2.1. Then A can be obtained as

$$A = \frac{\pi^2 D_0}{4d^2} \tag{2.15}$$

However, the obtained D_0 from equation 2.15 cannot be used as a pre-exponential factor of the apparent diffusivity, since the D_{app} is clearly not a form of $A \exp(B/T)$ and equation 2.14 does not consider the trapping but it is from diffusion only.

2.2.3 Summary

The TDS experimental technique which is one of the most useful methods to investigate the trapping phenomenon is introduced and related studies have been reviewed. In order to interpret the measured TDS data, Kissinger model (Choo & Lee, 1982; Kissinger, 1957), McNabb-Foster model (McNabb & Foster, 1963) and Oriani model (Oriani, 1970) have been utilized in the literature. The principles of each models and limitations were reviewed. In addition, the trap binding energies of various defects sites in ferritic and austenite steels have been surveyed from the previous research. Most of them was obtained from TDS experiments, but some were obtained from other techniques, such as permeation test (Hill & Johnson, 1959; Kumnick & Johnson, 1980; Pressouyre & Bernstein, 1978) and autoradiography (Asaoka *et al.*, 1977). However, those obtained binding energyies shows a large difference depending on the interpretation method.

References

ABRAHAM, D.P. & ALTSTETTER, C.J. (1995). The effect of hydrogen on the yield and flow stress of an austenitic stainless steel. *Metallurgical and Materials Transactions A*, **26**, 2849–2858. 7

ASAOKA, T., DAGBERT, C., AUCOUTURIER, M. & GALLAND, J. (1977). Quantitative study of trapping characteristics of H in a Fe-0.15Ti ferrite by high-resolution autoradiography and during regassing at high temperatures. *Scripta Materialia*, **11**, 467–472. 10, 11, 16

BARNOUSH, A. & VEHOFF, H. (2008). Hydrogen embrittlement of aluminum in aqueous environments examined by in situ electrochemical nanoindentation. *Scripta Materialia*, **58**, 747–750. 7

BARNOUSH, A. & VEHOFF, H. (2010). Recent developments in the study of hydrogen embrittlement: hydrogen effect on dislocation nucleation. *Acta Materialia*, **58**, 5274–5285. 7

BARNOUSH, A., DAKE, J., KHERADMAND, N. & VEHOFF, H. (2010). Examination of hydrogen embrittlement in feal by means of in situ electrochemical micropillar compression and nanoindentation techniques. *Intermetallics*, **18**, 1385–1389. 7

BASTIEN, P. & AZOU, P. (1951). Effect of hydrogen on the deformation and fracture of iron and steel in simple tension. In *Proceedings of the First World Metallurgical Congress*, 535. 4

BEACHEM, C. (1972). A new model for hydrogen-assisted cracking (hydrogen embrittlement). *Metallurgical Transactions*, **3**, 441–455. 5, 7

BIRNBAUM, H.K. & SOFRONIS, P. (1994). Hydrogen-enhanced localized plasticitya mechanism for hydrogen-related fracture. *Materials Science and Engineering: A*, **176**, 191–202. 5, 7

17

CHOO, W. & LEE, J.Y. (1982). Thermal analysis of trapped hydrogen in pure iron. *Metallurgical Transactions A*, **13**, 135–140. 9, 10, 11, 12, 16

CHORNET, E. & COUGHLIN, R.W. (1972). Chemisorption of hydrogen on iron. *Journal of Catalysis*, **27**, 246–265. 11

COTTRELL, A. & JASWON, M. (1949). Distribution of solute atoms round a slow dislocation. *Proceedings of the Royal Society of London. Series A. Mathematical and Physical Sciences*, **199**, 104–114. 7

DARKEN, L.S. & SMITH, R.P. (1949). Behavior of hydrogen in steel during and after immersion in acid. *Corrosion*, **5**, 1–16. 8

DAYAL, R. & PARVATHAVARTHINI, N. (2003). Hydrogen embrittlement in power plant steels. *Sadhana*, **28**, 431–451. 4

EBIHARA, K.I., SUZUDO, T., KABURAKI, H., TAKAI, K. & TAKE-BAYASHI, S. (2007). Modeling of hydrogen thermal desorption profile of pure iron and eutectoid steel. *ISIJ international*, **47**, 1131–1140. 13

EBIHARA, K.I., KABURAKI, H., SUZUDO, T. & TAKAI, K. (2009). A numerical study on the validity of the local equilibrium hypothesis in modeling hydrogen thermal desorption spectra. *ISIJ international*, **49**, 1907–1913. 13

ENOMOTO, M., HIRAKAMI, D. & TARUI, T. (2006). Modeling thermal desorption analysis of hydrogen in steel. *ISIJ international*, **46**, 1381–1387. 13

FERREIRA, P., ROBERTSON, I. & BIRNBAUM, H. (1998). Hydrogen effects on the interaction between dislocations. *Acta Materialia*, **46**, 1749–1757. 7

18

GAHR, S., GROSSBECK, M. & BIRNBAUM, H. (1977). Hydrogen embrittlement of Nb I – macroscopic behavior at low temperatures. *Acta Metallurgica*, **25**, 125–134. 5

GERBERICH, W., MARSH, P. & HOEHN, J. (1996). Hydrogen induced cracking mechanisms–are there critical experiments? *Hydrogen Effects in Materials*, 539–554. 5

HANCOCK, G. & JOHNSON, H. (1966). Hydrogen, oxygen, and subcritical crack growth in a high-strength steel. *Trans. TMS–AIME.*, **236**, 513–516. 5

HILL, M. & JOHNSON, E. (1959). Hydrogen in cold worked iron-carbon alloys and the mechanism of hydrogen embrittlement. *Trans. metall. Soc. AIME*, **215**, 717–725. 11, 16

HIRTH, J.P. (1980). Effects of hydrogen on the properties of iron and steel. *Metallurgical Transactions A*, **11**, 861–890. 4

JOHNSON, W.H. (1874). On some remarkable changes produced in iron and steel by the action of hydrogen and acids. *Proceedings of the Royal Society of London*, **23**, 168–179. 4

KISSINGER, H.E. (1957). Reaction kinetics in differential thermal analysis. *Analytical Chemistry*, **29**, 1702–1706. 9, 10, 16

KO, W.S., JEON, J.B., SHIM, J.H. & LEE, B.J. (2012). Origin of hydrogen embrittlement in vanadium-based hydrogen separation membranes. *International Journal of Hydrogen Energy*, **37**, 13583–13593. 4

KUMNICK, A. & JOHNSON, H. (1980). Deep trapping states for hydrogen in deformed iron. *Acta Metallurgica*, **28**, 33–39. 11, 12, 16

LEE, H. & LEE, J.Y. (1984). Hydrogen trapping by TiC particles in iron. *Acta Metallurgica*, **32**, 131–136. 11, 12

LEE, J. & LEE, J.Y. (1983). Hydrogen trapping in AISI 4340 steel. *Metal Science*, **17**, 426–432. 11

LEE, J.L. & LEE, J.Y. (1986). The interaction of hydrogen with the interface of Al_2O_3 particles in iron. *Metallurgical Transactions A*, **17**, 2183–2186. 11

LEE, K., LEE, J.Y. & KIM, D. (1984). A study of hydrogen-trapping phenomena in AISI 5160 spring steel. *Materials Science and Engineering*, **67**, 213–220. 11

LOUTHAN JR, M., CASKEY JR, G., DONOVAN, J. & RAWL JR, D. (1972). Hydrogen embrittlement of metals. *Materials Science and Engineering*, **10**, 357–368. 4, 5

MCNABB, A. & FOSTER, P. (1963). A new analysis of the diffusion of hydrogen in iron and ferritic steels. *Trans. AIME*, **227**, 618. 9, 12, 16

MYERS, S.M., BASKES, M., BIRNBAUM, H., CORBETT, J.W., DELEO, G., ESTREICHER, S., HALLER, E.E., JENA, P., JOHNSON, N.M., KIRCHHEIM, R. *et al.* (1992). Hydrogen interactions with defects in crystalline solids. *Reviews of Modern Physics*, **64**, 559. 7

NAGUMO, M. (2004). Hydrogen related failure of steels–a new aspect. *Materials Science and Technology*, **20**, 940–950. 5

NINGSHEN, S., UHLEMANN, M., SCHNEIDER, F. & KHATAK, H. (2001). Diffusion behaviour of hydrogen in nitrogen containing austenitic alloys. *Corrosion Science*, **43**. 10

ONO, K. & MESHII, M. (1992). Hydrogen detrapping from grain boundaries and dislocations in high purity iron. *Acta Metallurgica et Materialia*, **40**, 1357–1364. 10, 11

ORIANI, R. & JOSEPHIC, P. (1974). Equilibrium aspects of hydrogen-induced cracking of steels. *Acta metallurgica*, **22**, 1065–1074. 5

ORIANI, R.A. (1970). The diffusion and trapping of hydrogen in steel. *Acta Metallurgica*, **18**, 147–157. 9, 11, 13, 16

PARK, Y., MAROEF, I., LANDAU, A. & OLSON, D. (2002). Retained austenite as a hydrogen trap in steel welds. *Weld. Journal-New York-*. 10

PÉREZ ESCOBAR, D., MIÑAMBRES, C., DUPREZ, L., VERBEKEN, K. & VERHAEGE, M. (2011). Internal and surface damage of multiphase steels and pure iron after electrochemical hydrogen charging. *Corrosion Science*, **53**, 3166–3176. iv, 5, 6

PETCH, N. & STABLES, P. (1952). Delayed fracture of metals under static load. *Nature*, **169**, 842–843. 5

PODGURSKI, H. & ORIANI, R. (1972). Nitrogenation of Fe-Al alloys. III: Absorption of hydrogen in nitrogenated Fe-Al alloys. *Metallurgical Transactions*, **3**, 2055–2063. 11

PRESSOUYRE, G. & BERNSTEIN, I. (1978). A quantitative analysis of hydrogen trapping. *Metallurgical Transactions A*, **9**, 1571–1580. 11, 16

ROBERTSON, I. (2001). The effect of hydrogen on dislocation dynamics. *Engineering Fracture Mechanics*, **68**, 671–692. 5, 7

ROBERTSON, W.M. & THOMPSON, A.W. (1980). Permeation measurements of hydrogen trapping in 1045 steel. *Metallurgical Transactions A*, **11**, 553–557. 13

ROGERS, H. (1968). Hydrogen embrittlement of metals atomic hydrogen from a variety of sources reduces the ductility of many metals. *Science*, **159**, 1057–1064. 5

RYU, J.H. (2012). *Hydrogen embrittlement in TRIP and TWIP steels*. Ph.D. thesis, Pohang university of Science and Technology, Korea. iv, 9

SAN-MARTIN, A. & MANCHESTER, F. (1990). The Fe-H (iron-hydrogen) system. *Bulletin of Alloy Phase Diagrams*, **11**, 173–184. 8

SO, K., KIM, J., CHUN, Y., PARK, K., LEE, Y. & LEE, C. (2009). Hydrogen delayed fracture properties and internal hydrogen behavior of a Fe-18Mn-1.5 Al-0.6C TWIP steel. *ISIJ international*, **49**, 1952–1959. 10

SOFRONIS, P. & ROBERTSON, I. (2002). Transmission electron microscopy observations and micromechanical/continuum models for the effect of hydrogen on the mechanical behaviour of metals. *Philosophical Magazine A*, **82**, 3405–3413. 7

SONG, J. & CURTIN, W. (2013). Atomic mechanism and prediction of hydrogen embrittlement in iron. *Nature materials*, **12**, 145–151. 4

TAKAI, K. & WATANUKI, R. (2003). Hydrogen in trapping states innocuous to environmental degradation of high-strength steels. *ISIJ international*, **43**, 520–526. 12

TAKETOMI, S., MATSUMOTO, R. & MIYAZAKI, N. (2008). Atomistic study of hydrogen distribution and diffusion around a {112}¡ 111¿ edge dislocation in alpha iron. *Acta Materialia*, **56**, 3761–3769. 4, 7

TETELMAN, A. & ROBERTSON, W. (1961). The mechanism of hydrogen embrittlement observed in iron-silicon single crystals. Tech. rep., DTIC Document. 4

TROIANO, A.R. (1960). The role of hydrogen and other interstitials in the mechanical behavior of metals. *Trans. ASM*, **52**, 54–80. 5

TURNBULL, A., HUTCHINGS, R. & FERRISS, D. (1997). Modelling of thermal desorption of hydrogen from metals. *Materials Science and Engineering: A*, **238**, 317–328. 13

VEHOFF, H. & ROTHE, W. (1983). Gaseous hydrogen embrittlement in FeSi-and Ni-single crystals. *Acta Metallurgica*, **31**, 1781–1793. iv, 5, 6

WALLAERT, E., DEPOVER, T., ARAFIN, M. & VERBEKEN, K. (2014). Thermal Desorption Spectroscopy Evaluation of the Hydrogen-Trapping Capacity of NbC and NbN Precipitates. *Metallurgical Materials Transactions A*, **45**, 2412–2420. 11

WEI, F., HARA, T. & TSUZAKI, K. (2004). Precise determination of the activation energy for desorption of hydrogen in two Ti-added steels by a single thermal-desorption spectrum. *Metallurgical and Materials Transactions B*, **35**, 587–597. 11, 12

WEI, F.G., ENOMOTO, M. & TSUZAKI, K. (2012). Applicability of the Kissingers formula and comparison with the Mcnabb–Foster model in simulation of thermal desorption spectrum. *Computational Materials Science*, **51**, 322–330. 15

WEN, M., FUKUYAMA, S. & YOKOGAWA, K. (2003). Atomistic simulations of effect of hydrogen on kink-pair energetics of screw dislocations in bcc iron. *Acta materialia*, **51**, 1767–1773. 4

XIUKUI, S., JIAN, X. & YIYI, L. (1989). Hydrogen permeation behaviour in austenitic stainless steels. *Materials Science and Engineering A*, **114**, 179–187. 10

YAMAGUCHI, T. & NAGUMO, M. (2003). Simulation of hydrogen thermal desorption under reversible trapping by lattice defects. *ISIJ international*, **43**, 514–519. 15

ZAPFFE, C. & SIMS, C. (1941). Hydrogen embrittlement, internal stress and defects in steel. *Trans. AIME*, **145**, 225–271. 4, 5

Chapter 3

Hydrogen Desorption in Single Phase Steel - Ferrite

3.1 Introduction

Hydrogen is a pernicious solute in iron in the sense that it leads to dramatic changes in the ability of the metal to absorb energy during fracture, at concentrations which are so small (Bhadeshia, 2012; Hirth, 1980) that it is difficult to avoid the ingress of nascent hydrogen during, for example, corrosion reactions. Studies of hydrogen embrittlement tend to be of two kinds, the first to characterize the potency of embrittlement, and the second relatively recent approach, to render it innocuous should it enter the steel (Hagihara *et al.*, 2012; Pérez Escobar *et al.*, 2012; Ryu *et al.*, 2012).

It is established that the passage of hydrogen through a steel is hindered by lattice imperfections which tend to attract and bind it, thus rendering it immobile at temperatures where it should normally be able to diffuse readily (Darken & Smith, 1949). This phenomenon, known as trapping, can be investigated using thermal desorption spectroscopy (TDS) which monitors the rate at which hydrogen is released from a

sample during continuous heating. Strong traps release their hydrogen at higher temperatures and data such as these can be used to probe the parameters defining the interaction of hydrogen with defects. The technique is nevertheless indirect so the interpretation of the curve of desorption rate versus temperature and heating rate requires interpretation. The methods and their limitations are reviewed in the previous chapter. Also, the interpretation becomes more difficult due to the overlapping of the desorption peaks which caused from different kinds of traps, for example, dislocations, grain boundaries or different phase. In this chapter, aspects of the available theory are incorporated into a new numerical model which permits more complex problems to be resolved, for example the role of multiple trapping centers. The method is then validated using new experimental data and an assessment of published data from the literature.

3.2   Numerical Analysis of Hydrogen Desorption

To cope with the limitations of the methods described in the previous chapter, a numerical finite difference method was programmed. It is important to emphasis that the method permits multiple binding sites, and it can deal with the unsaturated sample. It is assumed that there is no interaction between the trapped and free hydrogen and that one-dimensional diffusion occurs through the lattice in a direction normal to the plane of a steel sheet. Hydrogen is first introduced into the sample and distributed between the trap sites and lattice sites either assuming local equilibrium based on the Oriani's work (Oriani, 1970) or via a kinetic model based on the McNabb and Foster scheme (McNabb & Foster, 1963). The lattice hydrogen is then allowed to diffuse out to the free surface using a finite difference method (FDM). This process is repeated until the sample reaches the target temperature, Fig. 3.1. There are two processes during the simulation, one is the diffusion through the lattice, Fig. 3.2a

and the other is the trapping/detrapping between the lattice and trap sites, Fig. 3.2b.
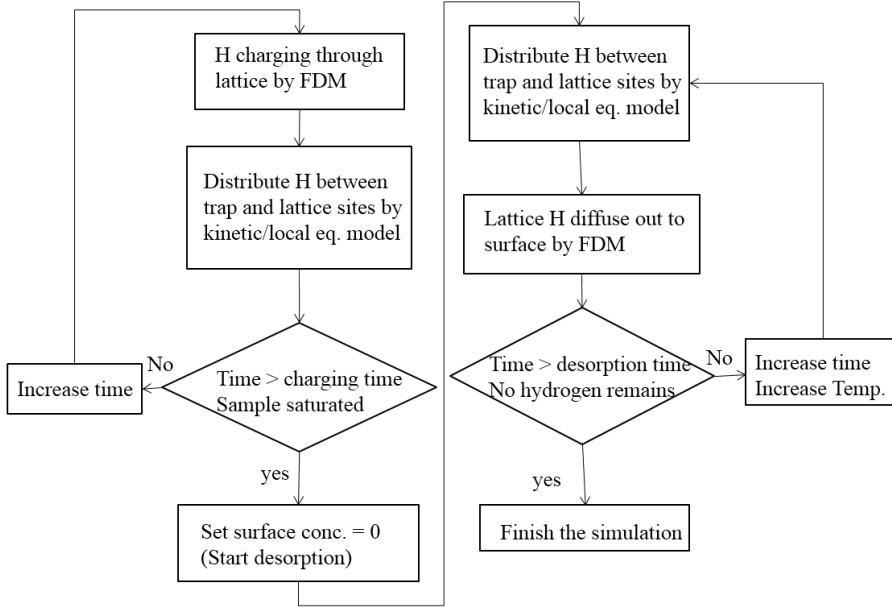
Figure 3.1: Flow chart illustrating the numerical calculation process.

Using symmetry it is only necessary to model half of the specimen, which for 1 mm length was divided into 50 elements after demonstrating that further subdivision did not make a significant difference to the calculated outcomes. In the case of austenite where diffusion is much slower, the number of elements per mm was increased to 800. Hydrogen is first introduced into the sample assuming a fixed surface concentration. The time interval was chosen to be less than $\frac{1}{3}(\Delta z)^2 D^{-1}$, where Δz is the dimension of the FDM element. For the effusion part of the process which begins when charging is halted, the hydrogen concentration at the surface is set to zero, assuming that any interfacial reaction effects can be neglected (Kleimt *et al.*, 2000). The software for doing these calculations, together with examples of inputs and outputs, and documentation

26
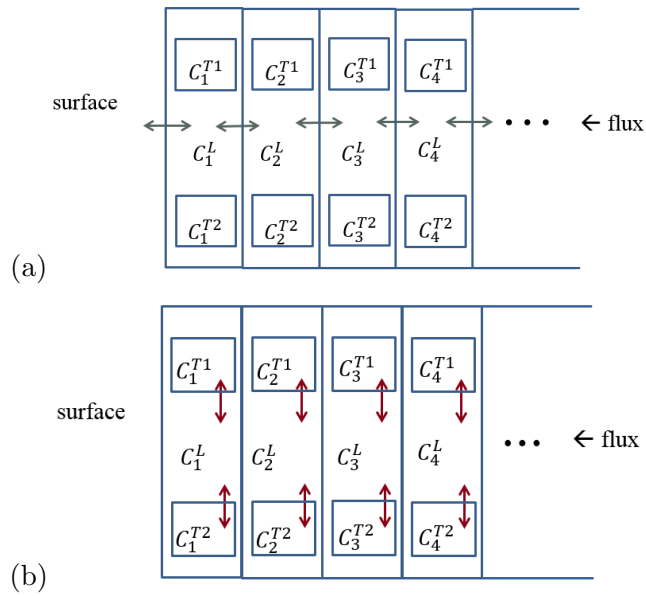
Figure 3.2: The schematic diagram for the (a) hydrogen diffusion through the lattice sites and (b) the trapping/detrapping between the lattice and trap sites. Two kinds of trap sites are assumed in this diagram.

is available freely on :

http://www.msm.cam.ac.uk/map/steel/programs/hydrogen.html

3.2.1   Kinetic Model

Here we adapt a model which accounts for the capture and release of hydrogen from traps, and diffusion through the lattice (McNabb & Foster, 1963), however, we modified the model so that many fitting parameters can be avoided. The chances ϕ_t of the trapping of hydrogen atom will be related to the respective activation energy and the fraction of unoccupied neighboring trap sites. In this case, the respective activation energy is the diffusion activation energy of hydrogen E_d. Also N_l and N_t are the densities of lattice and trap sites, respectively and θ_l and θ_t are the occupancies of lattice and trap sites, respectively. The occupancy can be defined as the concentration of hydrogen divided by the density of the respective sites.

$$\phi_t = \exp\left(\frac{E_d}{RT}\right) \frac{N_t(1-\theta_t)}{N_l(1-\theta_l) + N_t(1-\theta_t)} \tag{3.1}$$

Similarly the chances ϕ_d of the detrapping of hydrogen atoms will be related to the detrapping activation energy and the fraction of unoccupied neighboring lattice sites. For the detrapping, the respective activation energy is $E_d + E_b$.

$$\phi_d = \exp\left(\frac{E_d + E_b}{RT}\right) \frac{N_l(1-\theta_l)}{N_t(1-\theta_t) + N_l(1-\theta_l)} \tag{3.2}$$

During a time interval dt, a hydrogen atom will make $\nu \times dt$ attempts at the activation barrier, where ν is an attempt frequency, here assumed to be the Debye frequency of $10^{13}\,\mathrm{s}^{-1}$. It follows that probabilities p_t and

p_d of the trapping and detrapping events are given by

$$
\begin{aligned}
p_t &= 1 - (1 - \phi_t)^{dt\,\nu} \\
p_d &= 1 - (1 - \phi_d)^{dt\,\nu}
\end{aligned}
\tag{3.3}
$$

so that the instantaneous concentrations C_l' and C_t' at the lattice and trap sites become:

$$
\begin{aligned}
C_l' &= C_l(1 - p_t) + C_t p_d \\
C_t' &= C_l p_t + C_t(1 - p_d)
\end{aligned}
\tag{3.4}
$$

after the time interval dt. These concentrations are adjusted during each time step of the numerical scheme, thus accounting explicitly for the barriers to the trapping or detrapping events.

3.2.2 Local Equilibrium Model

Here we adapt a model which assumes local equilibrium between trapped and free hydrogen (Oriani, 1970), however, instead of using the apparent diffusivity we calculate the amount of trapped hydrogen itself so that we can avoid the assumption $\theta_t \ll 1$ which is not proper for the thermal desorption analysis. The amount of trapped hydrogen can be obtained from the mass conservation and local equilibrium.

$$
C_l + C_t = C_l' + C_t'
\tag{3.5}
$$

$$
\frac{\theta_t(1 - \theta_l)}{\theta_l(1 - \theta_t)} = \exp\left(\frac{E_b}{RT}\right)
\tag{3.6}
$$

 Equation (6) is from the assumptions that local equilibrium exists between the concentrations of hydrogen in the lattice and at traps, both for a static and dynamic population of hydrogen (i.e., during diffusion) and assuming no interactions between the occupied sites. The details are in the previous chapter 2. Then by solving the quadratic equation we can obtain the distribution of hydrogen on potential sites.

3.2.3 Comparison

3.2.3.1 Kinetic Model and Local Equilibrium Model

The numerical model based on the kinetic and local equilibrium approaches, was utilized to study ferritic steel sheet-samples of $2\,\text{mm}$ thickness, with heating rates of 100 and $200\,^\circ\text{C}\,\text{h}^{-1}$, a trap binding energy of $50\,\text{kJ}\,\text{mol}^{-1}$ and lattice-site density $2.6 \times 10^{29}\,\text{m}^{-3}$, trap density $2 \times 10^{24}\,\text{m}^{-3}$. The diffusivity of hydrogen in ferrite was $D_0 = 5.8 \times 10^8\,\text{m}^2\,\text{s}^{-1}$ and $E_d = 4.5\,\text{kJ}\,\text{mol}^{-1}$ (Hagi & Hayashi, 1987). The densities are estimated as follows. There are six tetrahedral interstices which can accommodate hydrogen, per iron atom in ferrite, however it was assumed that only the half of total tetrahedral sites are active because of the known repulsion between near neighbour hydrogen pairs in ferrite (Minot & Demangeat, 1985). Then

$$N_l = \frac{\text{Avogadro number}}{\text{molar volume}} \times 3 \tag{3.7}$$

Dislocations and grain boundaries are the trap sites expected in annealed ferritic steel. The trap density due to dislocations was assumed as

$$N_t^\rho = \pi r_d^2 \rho N_l \tag{3.8}$$

where r_d is the effective radius and taken to be equal to b, the magnitude of the dislocation Burgers vector; this is consistent with previous work that the hydrogen is essentially trapped in the core of dislocation rather than in its extended strain field (Ono & Meshii, 1992). Also, ρ is the dislocation density. The trap density due to grain boundaries was calculated as follows:

$$N_t^S = S_V r_d N_l \tag{3.9}$$

where $r_d = 2b$, and S_V is the grain boundary surface area per unit volume. As an example, the trap density for a sample with a dislocation density

of $10^{10}\,\mathrm{m}^{-2}$ and grain size $200\,\mu\mathrm{m}$, is about $2 \times 10^{24}\,\mathrm{m}^{-3}$ according to equations (8) and (9). It turns out that for the conditions studied, the results of the local equilibrium model and kinetic models are consistent, probably because the heating rate is not particularly large, so that an equilibrium distribution of hydrogen in maintained at all temperatures, Fig. 3.3. Since the computation time for kinetic model is much longer than the local equilibrium model, all the following simulation is done with the local equilibrium model.
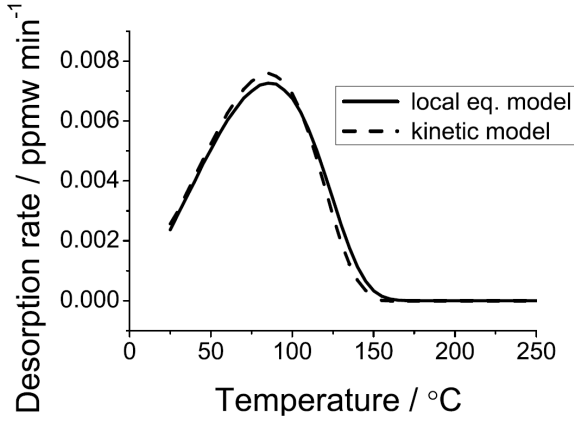
Figure 3.3: Results using both local equilibrium and kinetic models.

3.2.3.2   Present Model and Kissinger's Model

In order to compare this present model and Kissinger's model, the predicted TDS results from this model were analyzed by the Kissinger's model. The TDS results of ferritic samples with 1, 2, and 8 mm thickness, with heating rates of 50, 100, 200 °C h^{-1} were predicted with the same binding energy $50\,\mathrm{kJ\,mol^{-1}}$ and trap density $2 \times 10^{24}\,\mathrm{m}^{-3}$. The results are shown in Fig. 3.4. From those curves, the peak temperatures were obtained. Then the binding energy was obtained from the peak temperature change with the different heating rate. T_p is the peak temperature

Table 3.1: The trap binding energies(kJ mol^{-1}) from present model and Kissinger's model.

Sample thickness	Present model	Kissinger's model
1 mm	50	50
2 mm	50	57
8 mm	50	45

and π is the heating rate. The obtained binding energies were 50, 57, and 45 kJ mol^{-1} for the samples of thickness 1, 2, and 8 mm, respectively.

3.2.3.3 Present Model and Apparent Diffusivity Model

In order to compare this present model and Kissinger's model, the TDS curves were predicted from both present model and apparent diffusivity with different binding energy 40, 50, and 60 kJ mol^{-1} and other parameters are same for both cases. The heating rate was 100 °C h^{-1}, sample thickness was 2 mm, and trap density was 2×10^{24} m^{-3}. From the given binding energy and trap density, the apparent diffusivity was calculated at each temperature and based on the calculated diffusivity, hydrogen diffusion was simulated and the amount of trapped hydrogen is calculated from the local equilibrium and the initial hydrogen amount was same for both TDS curves from present model and Oriani's model. The results are shown in Fig. 3.6a. The main difference of the present model and apparent diffusivity is the $\theta_t \ll 1$ assumption in the latter. Then trap occupancy from this assumption θ_t^a can be obtained from equation (10) while the trap occupancy in the present model θ_t^p can be obtained from equation (11). Thus, $\theta_t^a > \theta_t^p$ holds and the desorption behavior is slower in apparent diffusivity model. The predicted TDS curves represent the hydrogen desorption after 45 min room temperature aging. The desorbed hydrogen during this aging process is larger in the results from the apparent diffusivity and it caused the maximum desorption increase.
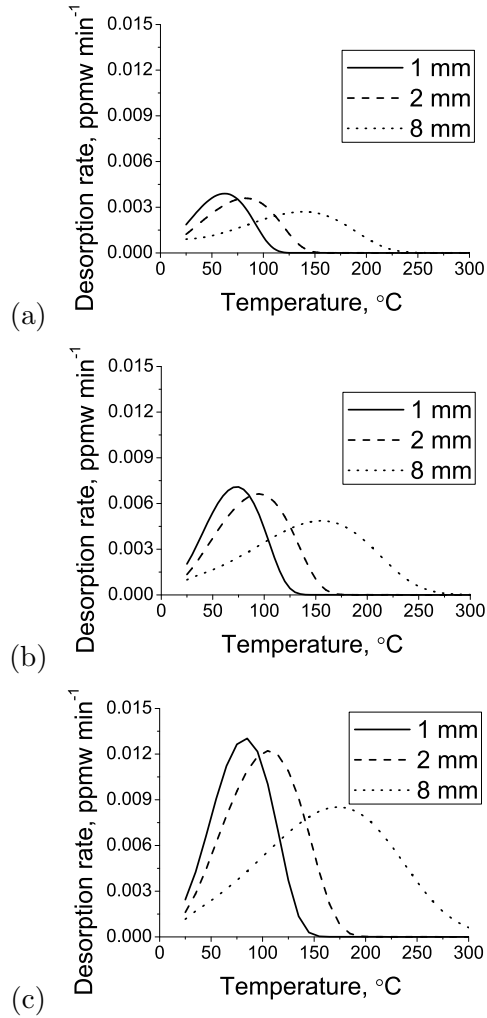
Figure 3.4: The simulated TDS curves with heating rate (a) $50\,^{\circ}\mathrm{C}\,\mathrm{h}^{-1}$, (b) $100\,^{\circ}\mathrm{C}\,\mathrm{h}^{-1}$ and (c) $200\,^{\circ}\mathrm{C}\,\mathrm{h}^{-1}$. For all the curves, trap binding energy and density are $50\,\mathrm{kJ}\,\mathrm{mol}^{-1}$ and $2 \times 10^{24}\,\mathrm{m}^{-3}$, respectively.
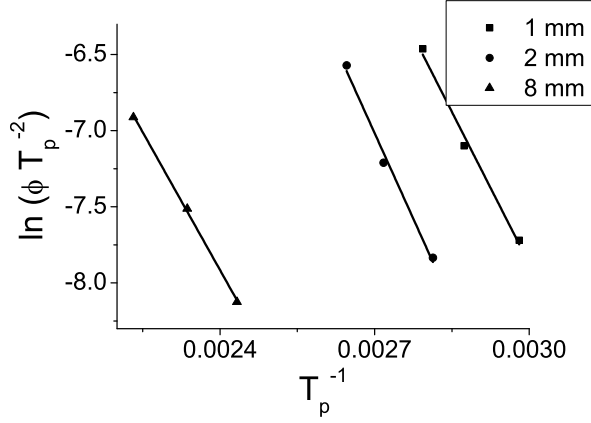
Figure 3.5: Peak temperature change as a function of heating rate.

$$\theta_t^a = \exp\left(\frac{E_b}{RT}\right)\theta_l \qquad (3.10)$$

$$\theta_t^p = \frac{\exp\left(\frac{E_b}{RT}\right)}{1 + \exp\left(\frac{E_b}{RT}\right)}\theta_l \qquad (3.11)$$

Also the sample with multiple traps is predicted with the present model and apparent diffusivity model. It was assumed that the sample has traps with binding energies 45 and $60\,\mathrm{kJ\,mol^{-1}}$, with the same trap density $2 \times 10^{24}\,\mathrm{m^{-3}}$ for each trap. The results are shown in Fig. 3.6b. From the present model, the two different peaks which correspond to the different trap were obtained, however the apparent diffusivity model can only predict one peak. Also, the evolution behavior was much slower in the apparent diffusivity model.

3.2.4 The Parameter Sensitivity

The numerical model described above was used to explore tendencies in TDS data, with concentration units in parts per million by weight (ppmw)

(a)

(b)
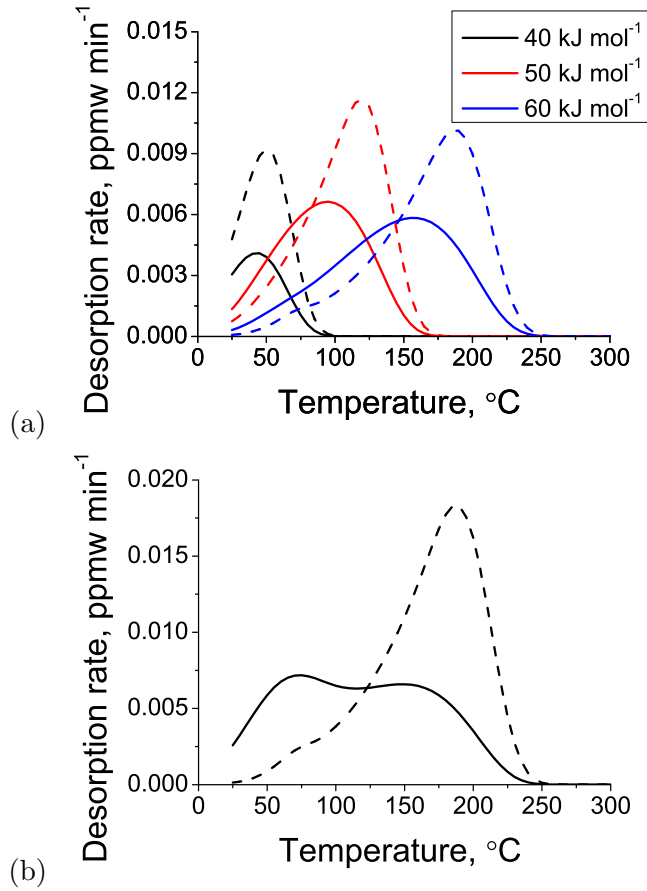
Figure 3.6: Predicted TDS curves from the present model (solid lines) and the apparent diffusivity model (dashed lines) with (a) different binding energies and (b) multiple traps.

equal to 1. The basis parameters used for the calculations include diffusivity as in the reference (?), steel thickness $l = 2\,\mathrm{mm}$, $E_b = 50\,\mathrm{kJ\,mol^{-1}}$, $N_t = 2 \times 10^{24}\,\mathrm{m^{-3}}$, $100\,^{\circ}\mathrm{C\,h^{-1}}$; diffusible hydrogen was allowed to evolve for 20 min prior to the generation of the TDS curves. A constant surface concentration of 0.1 ppmw was used in this case, however the effect of the surface concentration at charging is negligible on the TDS results as shown in later. Calculations were conducted to see the effects of these parameters would have on the effusion of hydrogen from the sample.

Fig. 3.7 and Fig. 3.8 show a variety of plots which illustrate trends. Stronger binding energy shifts the TDS curves to greater temperatures, Fig. 3.7a. As trap density increases, total hydrogen evolution and the maximum desorption rate increase and peak shifts to higher temperature. Note that this peak shift is not caused from higher binding energy but from that hydrogen needs more time to effuse because of the larger trap density, Fig. 3.7b. As might be expected from the longer diffusion distances, an increase in steel thickness causes more of the hydrogen to evolve at higher temperatures and extends the temperature range over which the effusion occurs, Fig. 3.8a. As the hydrogen concentration at lattice changes from 0.01 to 1.0 ppmw no significant difference in the TDS curves was predicted Fig. 3.8b. It is because the trap is saturated with the given binding energy and trap density, so the trapped hydrogen amount is not affected by the amount at lattice sites. As heating rate increases, the peak shifts to higher temperature, and the area under the curve increases. However, it is not related to the total hydrogen amount change since the hydrogen amount is obtained as the area under the curve divided by the heating rate, Fig. 3.8c.

An interesting set of results is presented in Fig. 3.9, for multiple traps, a scenario which cannot be modelled by the apparent diffusivity approach which can only deal with a single TDS peak; the approach presented here can deal with arbitrary numbers of traps. The calculations use the following parameters: case 1 has traps with binding energies 45 and $60\,\mathrm{kJ\,mol^{-1}}$,

(a)

(b)
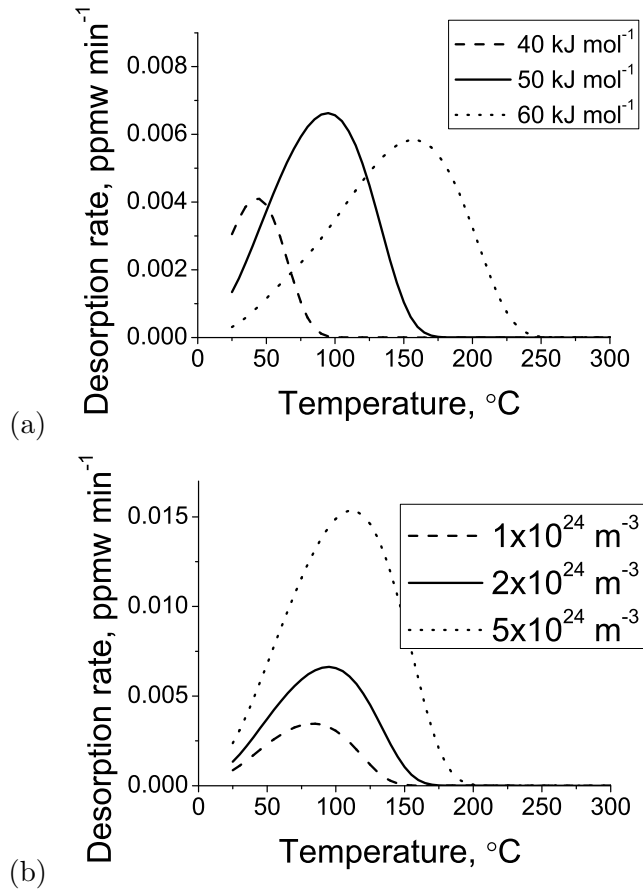
Figure 3.7: Effects of trap parameters on the TDS results; (a) binding energy and (b) trap density.
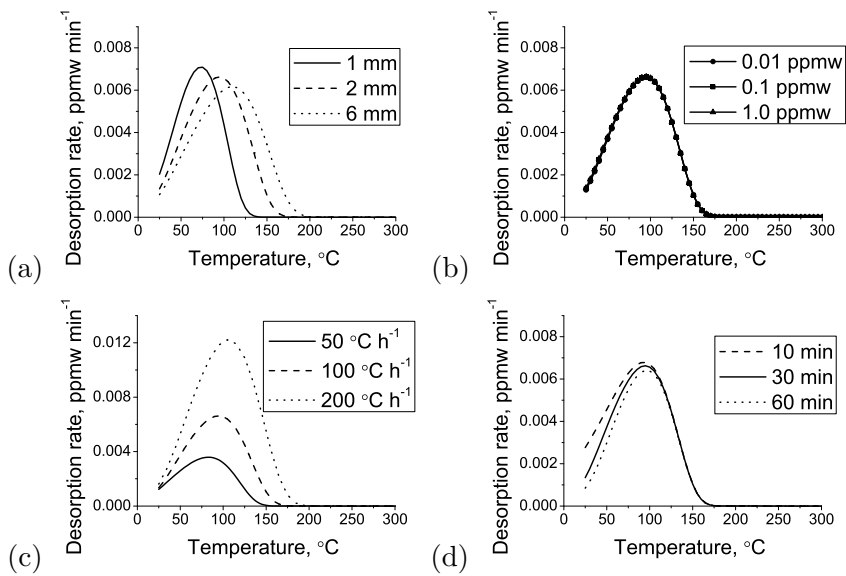
Figure 3.8: Effects of parameters on the TDS results; (a) sample thickness, (b) lattice hydrogen concentration at the surface, (c) heating rate, and (d) room temperature aging time.

with trap densities 5×10^{24} and $2 \times 10^{24} \, \text{m}^{-3}$ respectively, with the other conditions are same as for the reference condition. The only difference with case 2 is that the binding energies are changed to 47 and $55 \, \text{kJ} \, \text{mol}^{-1}$. Fig. 3.9a shows that for the conditions studied, a relatively large difference in the binding energies of the two kinds of traps leads to a curve (case 1) in which hydrogen evolution effectively occurs in two stages, whereas a smaller difference leads to overlap of the detrapping events from the two traps and hence an apparently simple peak shape. This interpretation is confirmed from the plot (Fig. 3.9b) of the hydrogen concentrations at different locations within the specimen. Fig. 3.9b, the lattice hydrogen comes entirely from detrapping from the two defects which bind the hydrogen. The hydrogen from the less potent trap is exhausted by about 150°C, however, the hydrogen from the more potent trap is exhausted by about 200°C.

3.3 The Effects of Plastic Strain

3.3.1 Experimental

The aim was to measure the effects of the plastic strain on hydrogen desorption and to analyze the results with the numerical model. The chemical composition of the steel was Fe-0.004C-0.078Mn-0.015Cr-0.046Al-0.015Ti wt%.

In order to reduce the effect from pre-existing dislocations and grain boundaries, the steel was heat treated at 950 °C for 10 min with heating and cooling rates of $\pm \, 10 \, ^\circ\text{C} \, \text{s}^{-1}$. Tensile test samples were then cut into 50 mm guage length, 12.5 mm width and 0.7 mm thickness and plastically deformed to elongations of 10 % and 20 %.

The specimens were then polished with 800 grit sand papers, and charged electrochemically with hydrogen for 12 h using 3 % NaCl + 0.3 % NH$_4$SCN solution with $1 \, \text{A} \, \text{m}^{-2}$. This charging period is sufficient to sat-
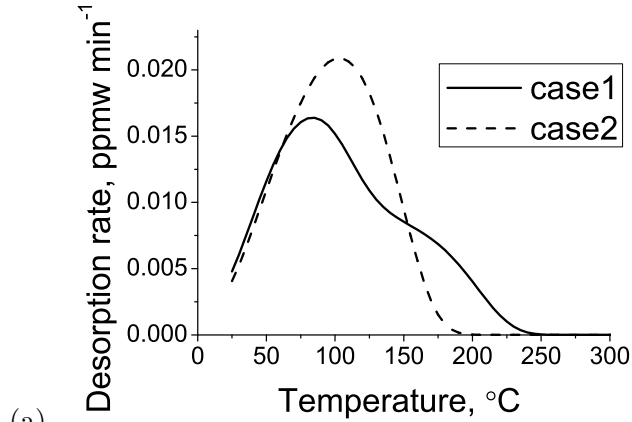
(a)
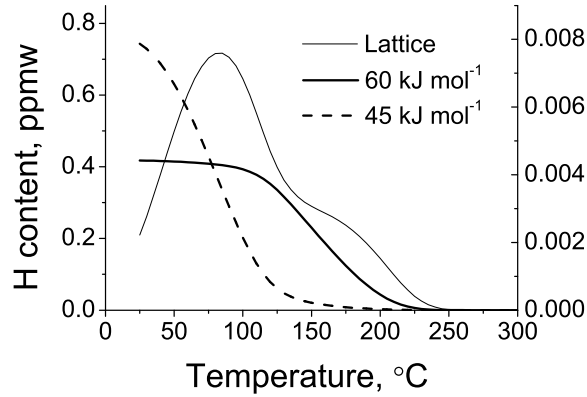
(b)

Figure 3.9: Calculated TDS results when two different trapping sites are present; case 1 is when binding energy difference is large, whereas the other case involves binding energies with smaller difference. (b) Calculated profile for case 1. The vertical scale on the right hand side refers to lattice hydrogen and that on the left to trapped hydrogen.

40

urate the samples. TDS experiments started within 30 min after the hydrogen charging was completed. The heating rate was 100 and 200 °C h^{-1}. The results were analyzed at 3 min intervals using helium as a carrier gas. The desorption rate was defined as the amount of hydrogen that evolves in 1 min. A standard mixture He + 10.2 volume ppm H$_2$ was used for calibrating the equipment. During the TDS experiment, the temperature is monitored via the equipment; therefore conducted calibration experiments were conducted by attaching a thermocouple to the sample itself, and relating the directly measured temperature to that output by the TDS equipment.

Fig. 3.10a shows the microstructure after the heat treatment. The grain size was obtained as $120.3 \pm 19.6 \, \mu$m by using the lineal intercepts method. The Vickers hardness of the undeformed steel determined with a load of 1 kg was 69 ± 2 HV1. Fig. 3.10b shows the stress-strain curve. The dislocation density of the deformed steel was estimated by converting the tensile stress into a shear stress τ :

$$\tau = \tau_0 + \alpha G b \sqrt{\rho} \tag{3.12}$$

where α is a numerical constant with value of 0.3   0.6, G is the shear modulus (81.7 GPa) and b is the magnitude of the dislocation Burgers vector, equal to 0.287 nm for ferrite. The calculated dislocation density changes for 10, 20% deformed sample are $3.53 \times 10^{13}, 6.31 \times 10^{13} \, \mathrm{m}^{-2}$ with $\tau_0 = 48.5$ MPa (calculated as half the tensile stress at yielding in Fig. 3.10b), $\alpha = 0.6$. It has been reported that for annealed iron, the measured dislocation density is practically zero when compared with that after implementation of plastic strains of the magnitudes considered here (**?**), so it has been assumed that the undeformed sample contains $\rho = 10^{10} \, \mathrm{m}^{-2}$.

Table 3.2: The obtained dislocation densities (m^{-2}).

Sample	Dislocation density
10% deformed	3.53×10^{13}
20% deformed	6.31×10^{13}
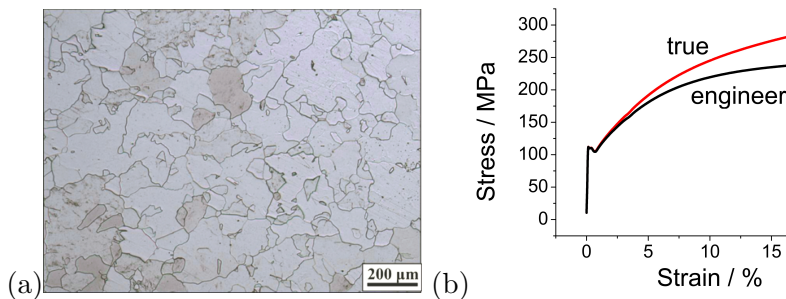
Figure 3.10: (a) Sample after heat treatment at 950°C for 10 min, (b) strain-stress curves.

3.3.2 Results and Discussions

The reversibility of hydrogen traps was investigated first. The charging and analysis were repeated three times with the maximum temperature on each occasion being 300 °C, but there was no significant change in the rate curves but slight decrease was observed as shown in Fig. 3.11.

The desorption rates for the plastically strained samples are shown at heating rates of 100 and 200 °C h^{-1}, respectively. The peak height increases with plastic strain, due presumably to the increasing dislocation density. The relation between the total hydrogen content and dislocation density is illustrated in Fig. 3.12.

The hydrogen content was obtained from the area under the curve in Fig. 3.12 divided by the heating rate and considered as a amount of hydrogen evolved after an interval of 30 min following hydrogen charging. The amount of hydrogen evolved after an interval of 15 and 30 min
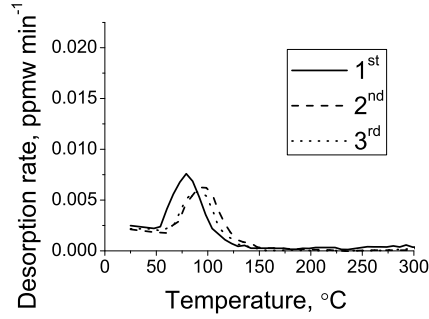
Figure 3.11: (a) Measured TDS data for repeated 3 times with the same sample when the heating rate is $100\,^{\circ}\mathrm{C}\,\mathrm{h}^{-1}$ and maximum temperature is $300\,^{\circ}\mathrm{C}$.

following hydrogen charging is shown in Fig. 5.5.

Analysis of the data first requires values for the binding energies and trap densities. Assuming grain boundaries and dislocations as traps, equations 8 and 9 were used to calculate the number density of each trap as a function of the grain size and dislocation density derived from the tensile test data as explained previously. The binding energies for the grain boundary trap sites was obtained by fitting to the TDS curve, that of 0% deformation sample heated at $100\,^{\circ}\mathrm{C}\,\mathrm{h}^{-1}$ and the binding energies for the dislocation trap sites was obtained by fitting to the TDS curve, that of 20% deformation sample heated at $100\,^{\circ}\mathrm{C}\,\mathrm{h}^{-1}$. Then the TDS curves with different heating rate, $200\,^{\circ}\mathrm{C}\,\mathrm{h}^{-1}$ were predicted by using the obtained trap binding energy and trap densities. However, the predicted TDS curves with $200\,^{\circ}\mathrm{C}\,\mathrm{h}^{-1}$ shows higher values than the measured data Fig. 3.14b and the misfit comes from the overestimated curve of the 0% deformed sample. After adjusting the trap density for grain boundary but the binding energy for grain boundary and dislocation, and the trap density for dislocation kept the same value, the TDS curves were predicted again. The comparisons between experimental and calculated results are shown in Fig. 3.14. The used binding energies and trap densities are in
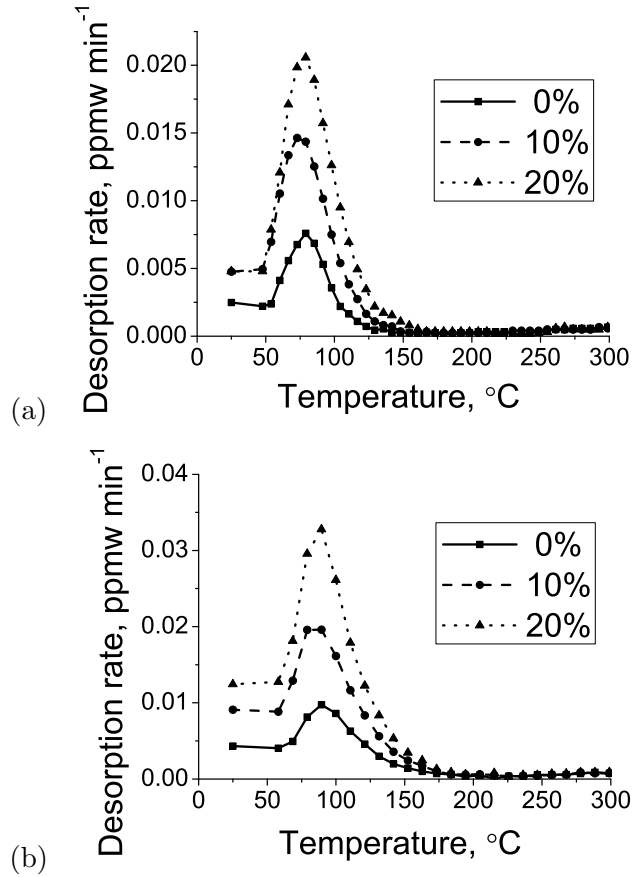
Figure 3.12: (a) Measured TDS data for heating rates of (a) 100 and (b) $200\,^{\circ}\mathrm{C}\,\mathrm{h}^{-1}$.
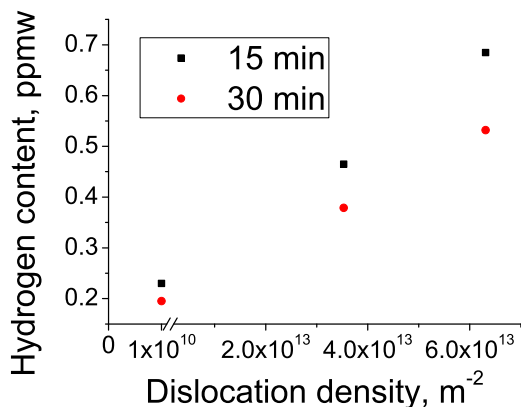
Figure 3.13: Total hydrogen content as a function of the dislocation density after 15 and 30 min from the hydrogen charging.

Table 3.3: The binding energies ($kJ \, mol^{-1}$) and trap densities ($10^{24} \, m^{-3}$) for the samples with heating rate $100 \, {}^{\circ}C \, h^{-1}$.

	0%	10%	20% deformed
grain boundary binding energy	53	53	53
grain boundary trap density	2.49	2.49	2.49
dislocation binding energy	48	48	48
dislocation trap density	0.0007	2.37	4.25

Table 3 and 4. Even though the reason why the TDS curve of 0% deformed sample shows different evolution with different heating rate is not clear, the predicted results for dislocation are in a good agreement with the measured data.

There are published data on flat specimens, of the effect of plastic deformation on hydrogen desorption from interstitial-free steel with grain size $30 \, \mu m$ and thickness $2 \, mm$ (Nagumo *et al.*, 1999). It is found that the data cannot be explained using the binding energies derived in the present work and the functions used to calculate trap densities, i.e., with-

45
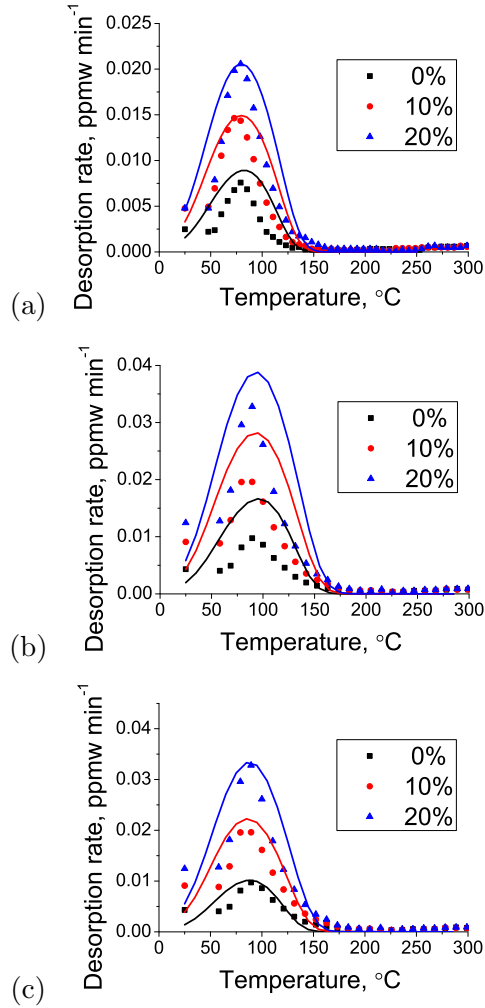
Figure 3.14: (a) Measured TDS data and predicted curves(solid lines) for heating rates of (a) 100 and (b) $200\,^\circ\text{C}\,\text{h}^{-1}$. The curves in (c) are the predicted results after the trap density for grain boundary was adjusted.

Table 3.4: The binding energies ($\mathrm{kJ\,mol^{-1}}$) and trap densities ($10^{24}\,\mathrm{m^{-3}}$) for the samples with heating rate $200\,^\circ\mathrm{C\,h^{-1}}$.

	undeformed	10% deformed	20% deformed
grain boundary binding energy	53	53	53
grain boundary trap density	1.5	1.5	1.5
dislocation binding energy	48	48	48
dislocation trap density	0.0007	2.37	4.25

out fitting. However, the direct application of the present work is difficult because of a lack of the information about dislocation density and the fact that the hydrogen evolution occurs at a lower temperature than is the case in our experiments, even though the specimens used by Nagumo and co-workers are thicker. Furthermore, the maximum desorption rates are lower in spite of the smaller 30 μm grain size reported for the sample studied. The reasons behind the discrepancies with our data are not clear.

There are further discrepancies when samples of pure iron are examined, where flat specimens heated at $60\,^\circ\mathrm{C\,h^{-1}}$ (Ono & Meshii, 1992), and cylindrical pieces heated at $100\,^\circ\mathrm{C\,h^{-1}}$ (Nagumo *et al.*, 1999) were studied. It was found that first hydrogen evolution peak in undeformed samples occurs at temperatures in the range 122-220 $^\circ$C, which are much greater than for the intersitial-free steel studied here, and indeed by Nagumo and co-workers (Nagumo *et al.*, 1999). The latter work was subsequently analysed using a numerical model by others (Ebihara *et al.*, 2007), but it was necessary to use a large binding energy of $61\,\mathrm{kJ\,mol^{-1}}$ in order to reproduce the approximate peak positions. This is a reflection of the experimental data for annealed pure iron are dramatically inconsistent with those for interstitial free steel, in that the hydrogen is strongly trapped. The literature has not commented on these discrepancies, which also cannot be resolved by the use of the present model without changing fitting

parameters.

It is also difficult to understand why in recent work, the TDS data for pure iron are insensitive to the amount of cold deformation (Pérez Escobar *et al.*, 2012); it has been suggested that this is because the hydrogen is weakly bound to dislocations but this does not seem reasonable in the context of ferritic iron where the binding energy is believed widely to be greater than the activation energy for diffusion (Hirth, 1980; Kumnick & Johnson, 1980). Hagi and Hayashi (Hagi & Hayashi, 1987) have tabulated data up to 1987, and in all cases the binding energy at dislocations is much greater than the activation energy for the diffusion of hydrogen. These data are all inconsistent with the experiments interpretation reported in (Pérez Escobar *et al.*, 2012). Our intention in highlighting these discrepancies is to stimulate further work in the future. Whereas there are clear inconsistencies in reported experimental data, some of the reported variations, for example, in the binding energy of hydrogen at dislocations, some 20-60 kJ mol^{-1} are undoubtedly due to approximations in the theoretical interpretations of the experimental data.

3.4 The Effects of Carbon Segregation

3.4.1 Experimental

The TDS curves of the sample before and after the baking process were compared to see the effects of carbon segregation on the hydrogen evolution. The chemical composition of the sample was Fe-0.01C-0.15Mn-0.0.07Si-0.03Cr-0.11Ni-0.05Al-0.05P wt%.

After heat-treated at 500 °C for 20 min, tensile test samples were cut into 50 mm guage length, 12.5 mm width and 0.7 mm thickness. The undeformed sample, 2% deformed sample, undeformed and baked sample, and 2% deformed and baked sample were prepared for the TDS experiments. The baking was conducted at 170 °C for 20 min. Each sample was

polished with 800 grit sand papers, and charged electrochemically with hydrogen for 12 h using 3 % NaCl + 0.3 % NH$_4$SCN solution with 1 A m^{-2}. TDS experiments started within 30 min after the hydrogen charging was completed. The heating rate was 100 and 200 °C h^{-1} and the temperature profile of the TDS curves reflects the actual temperature of the sample during heating.

3.4.2 Results and Discussions

The microstructure of the undeformed sample is shown in Fig. 3.15. The grain size of the as-received sample was measured by using the lineal intercepts method and the value was 10.3 ± 2.8 μm. Also, the effect of bake hardening can be confirmed from the strain-stress curve which indicates carbon is segregated during baking process (Baker *et al.*, 2002).
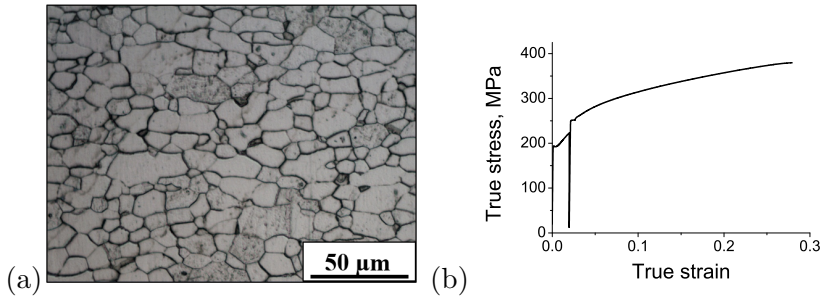
Figure 3.15: (a) Microstructure of the as-received sample and (b) the strain-stress curve.

The hydrogen thermal desorption results of 2% strained, and 2% strained and baked sample are shown in Fig. 3.16. Also the effect of baking was checked with the undeformed sample. The measured TDS curves of 0% deformed and after baked sample are shown in Fig. 3.17. For both cases, the peak temperature remains same but the decrease of hydrogen evolution was obtained after baking and from the results of undeformed sample, it was confirmed that baking process can reduce the

hydrogen absorption even without the plastic deformation. Indeed, the decrease in the TDS curves with the repeated sample (Fig. 3.17) might be related with the carbon segregation during the heating process for TDS. Given that dislocation recovery is sufficiently slow to prevent softening at given baking temperature, we can assume the trap density itself is same for the strained and after baking samples. Then the decrease of hydrogen evolution is suspected to be caused by the carbon segregation during the baking process.

(a)

(b)
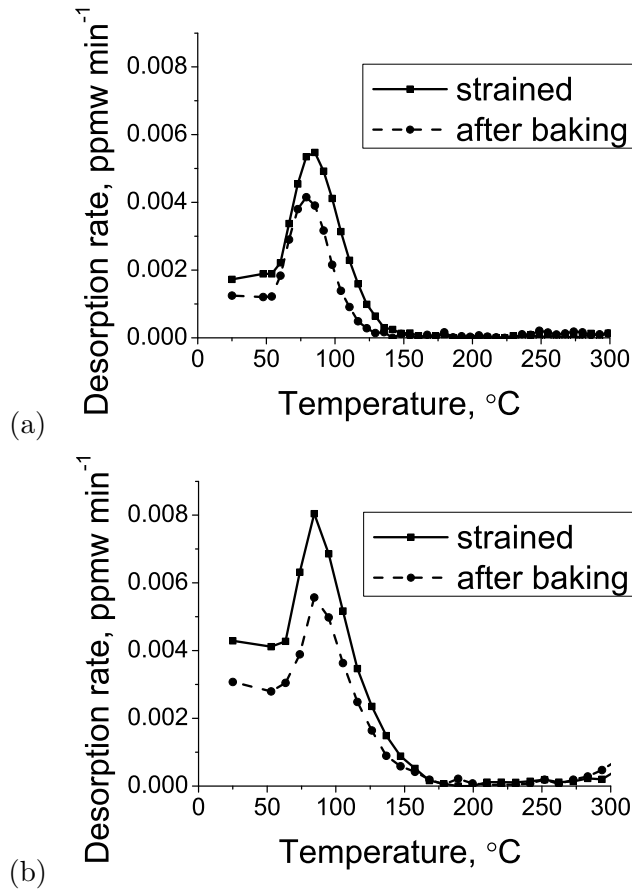
Figure 3.16: Measured TDS curves of pre-strained and after baking sample with heating rate of (a) 100 and (b) $200\,^{\circ}\mathrm{C\,h^{-1}}$.

(a)

(b)
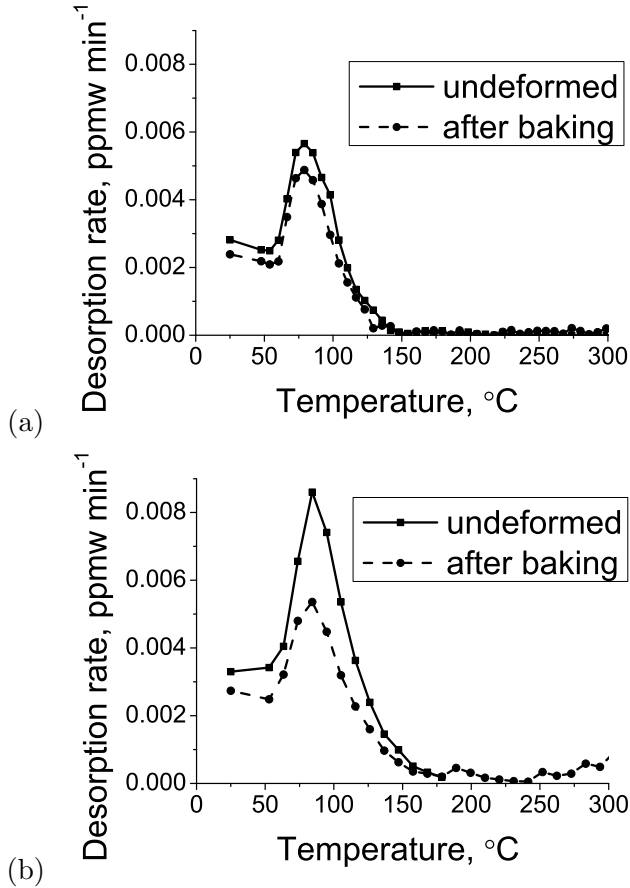
Figure 3.17: Measured TDS curves of undeformed and after baking sample with heating rate of (a) 100 and (b) $200\,^{\circ}\mathrm{C\,h^{-1}}$.

In order to analyze the effect of carbon segregation quantitatively, those curves were analyzed numerically. First, the dislocation density of 2% deformed sample was obtained from the equation (12) and the value was $5.5 \times 10^{11}\,\mathrm{m^2}$. Then from the equation (8), the trap density for dislocation was obtained to be $2.74 \times 10^{22}\,\mathrm{m^{-3}}$. From the TDS curve of 0% deformed sample, the trap density of grain boundary was fitted with the binding energy $53\,\mathrm{kJ\,mol^{-1}}$ which was obtained from the previous chapter. Then the trap densities for grain boundary are 1.6×10^{24} and

$1.3 \times 10^{24}\,\mathrm{m}^{-3}$ for heating rate of 100 and $200\,^{\circ}\mathrm{C}\,\mathrm{h}^{-1}$, respectively. The predicted and measured TDS curves for undeformed and 2% deformed samples are shown in Fig. 3.18. Since the dislocation density is very small, the contribution of dislocation density trapping in those curves is negligible. The parameters used are in Table 5 and 6 for the samples with heating rates 100 and $200\,^{\circ}\mathrm{C}\,\mathrm{h}^{-1}$, respectively.
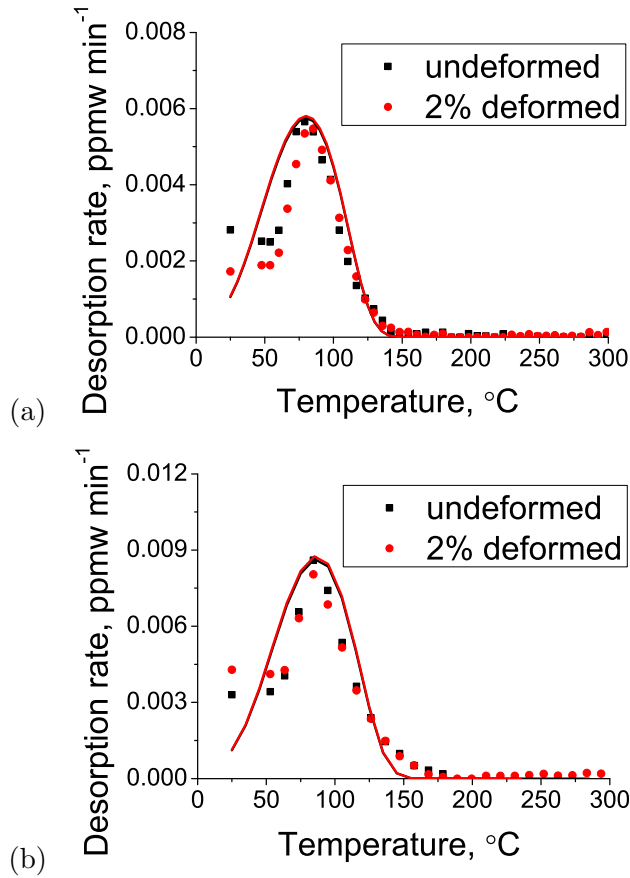
Figure 3.18: Measured TDS curves and predicted curves (solid lines) of undeformed and deformed sample with heating rate of (a) 100 and (b) $200\,^{\circ}\mathrm{C}\,\mathrm{h}^{-1}$.

(a)

(b)
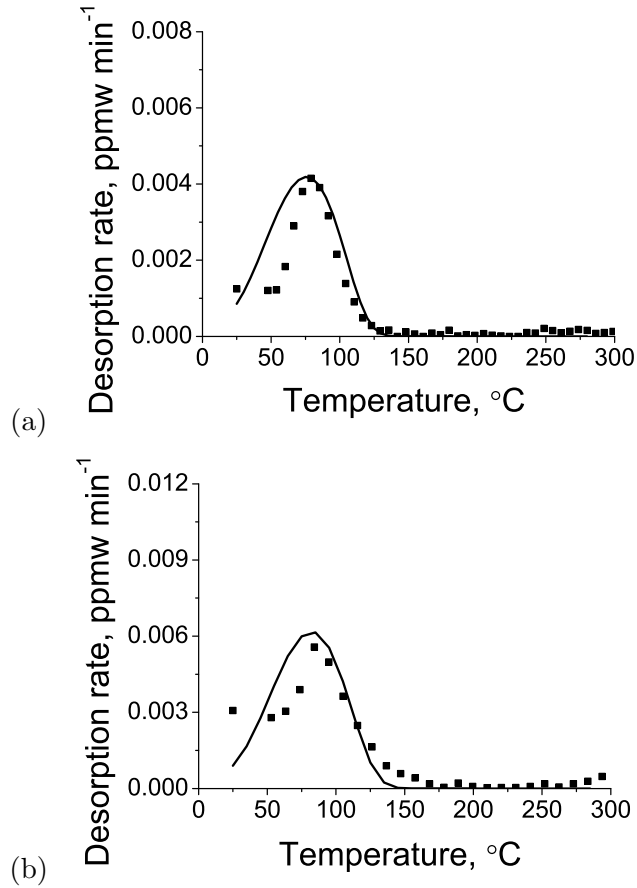
Figure 3.19: Measured TDS curves and predicted curves (solid lines) of strained and baked samples with heating rate of (a) 100 and (b) $200\,^\circ\mathrm{C\,h^{-1}}$.

Table 3.5: The binding energies ($kJ\,mol^{-1}$) and trap densities ($10^{24}\,m^{-3}$) for the samples with heating rate $100\,°C\,h^{-1}$.

	undeformed	2% deformed
grain boundary binding energy	53	53
grain boundary trap density	1.6	1.6
dislocation binding energy	48	48
dislocation trap density	0.0007	0.027

Table 3.6: The binding energies ($kJ\,mol^{-1}$) and trap densities ($10^{24}\,m^{-3}$) for the samples with heating rate $200\,°C\,h^{-1}$.

	undeformed	2% deformed
grain boundary binding energy	53	53
grain boundary trap density	1.3	1.3
dislocation binding energy	48	48
dislocation trap density	0.0007	0.027

By reducing the trap density 72% for curves with both heating rate 100 and $200\,°C\,h^{-1}$, the TDS curves for baked samples were predicted. The results are shown in Fig. 3.19. The baking process reduces the trap density of the sample about 72% by carbon segregation while the trap binding energy remains same. Although the carbon segregation to grain boundary during baking process have been reported (Baker *et al.*, 2002), there is a need to check the carbon segregation phenomenon and the residual stress before and after baking process should be checked.

3.5   Summary

A new numerical method that incorporates the local equilibrium and detrapping kinetics has been implemented to account for the real complexity of practical experiments. This model considers both diffusion and

trapping behavior and can deal with several kinds of trap sites and has been tested against new experimental data. From those analysis, the trap binding energies of the grain boundary and dislocation were found to be 53 and $48\,\mathrm{kJ\,mol^{-1}}$. However, when this new model was applied to the literature data, significant discrepancies were found. In particular, comparisons made between the trapping of hydrogen in pure iron and interstitial-free steel indicate a much stronger binding energy for hydrogen in the former case.

The effects of carbon segregation were also investigated by using a bake hardening steel. The TDS curves before and after the baking process were analyzed with the obtained binding energies. It was found that carbon segregation reduces the trap density about 72% but does not lead to a difference in the trap binding energy. However, the relationship between grain size and the amount of hydrogen which is trapped at grain boundary is not clear and the trap density for grain boundaries was obtained from the fitting.

References

BAKER, L., DANIEL, S. & PARKER, J. (2002). Metallurgy and processing of ultralow carbon bake hardening steels. *Materials Science and Technology*, **18**, 355–368. 49, 54

BHADESHIA, H. (2012). Steels for bearings. *Progress in materials Science*, **57**, 268–435. 24

DARKEN, L.S. & SMITH, R.P. (1949). Behavior of hydrogen in steel during and after immersion in acid. *Corrosion*, **5**, 1–16. 24

EBIHARA, K.I., SUZUDO, T., KABURAKI, H., TAKAI, K. & TAKEBAYASHI, S. (2007). Modeling of hydrogen thermal desorption profile of pure iron and eutectoid steel. *ISIJ international*, **47**, 1131–1140. 47

HAGI, H. & HAYASHI, Y. (1987). Effect of dislocation trapping on hydrogen and deuterium diffusion in iron. *Trans. Jpn. Inst. Met*, **28**, 368–374. 30, 48

HAGIHARA, Y., SHOBU, T., HISAMORI, N., SUZUKI, H., TAKAI, K.I. & HIRAI, K. (2012). Delayed fracture using CSRT and hydrogen trapping characteristics of V-bearing high-strength steel. *ISIJ international*, **52**, 298–306. 24

HIRTH, J.P. (1980). Effects of hydrogen on the properties of iron and steel. *Metallurgical Transactions A*, **11**, 861–890. 24, 48

KLEIMT, B., KÖHLE, S., JOHANN, K., JUNGREITHMEIER, A. & MOLINERO, J. (2000). Dynamic process model for denitrogenation and dehydrogenation by vacuum degassing. *Scandinavian Journal of Metallurgy*, **29**, 194–205. 26

KUMNICK, A. & JOHNSON, H. (1980). Deep trapping states for hydrogen in deformed iron. *Acta Metallurgica*, **28**, 33–39. 48

McNABB, A. & FOSTER, P. (1963). A new analysis of the diffusion of hydrogen in iron and ferritic steels. *Trans. AIME*, **227**, 618. 25, 28

MINOT, C. & DEMANGEAT, C. (1985). Binding energy of a pair of hydrogen atoms in α-iron. *Physics Letters A*, **108**, 285–288. 30

NAGUMO, M., TAKAI, K. & OKUDA, N. (1999). Nature of hydrogen trapping sites in steels induced by plastic deformation. *Journal of Alloys and Compounds*, **293**, 310–316. 45, 47

ONO, K. & MESHII, M. (1992). Hydrogen detrapping from grain boundaries and dislocations in high purity iron. *Acta Metallurgica et Materialia*, **40**, 1357–1364. 30, 47

ORIANI, R.A. (1970). The diffusion and trapping of hydrogen in steel. *Acta Metallurgica*, **18**, 147–157. 25, 29

PÉREZ ESCOBAR, D., DEPOVER, T., DUPREZ, L., VERBEKEN, K. & VERHAEGE, M. (2012). Combined thermal desorption spectroscopy, differential scanning calorimetry, scanning electron microscopy and X-ray diffraction study of hydrogen trapping in cold deformed trip steel. *Acta Materialia*, **60**, 2593–2605. 24, 48

RYU, J.H., CHUN, Y.S., LEE, C.S., BHADESHIA, H. & SUH, D.W. (2012). Effect of deformation on hydrogen trapping and effusion in trip-assisted steel. *Acta Materialia*, **60**, 4085–4092. 24

Chapter 4

Hydrogen Desorption in Single Phase Steel - TWIP

4.1 The Effects of Aluminum Addition

4.1.1 Introduction

It is established that high-manganese twinning-induced plasticity (TWIP) steels exhibit combinations of elongation and strength that are attractive for many potential applications, but particularly in the automotive industries (Bouaziz *et al.*, 2008; Frommeyer *et al.*, 2003; Remy & Pineau, 1977). However, some variants of TWIP alloys are susceptible to hydrogen-induced failure (Chin *et al.*, 2011; Koyama *et al.*, 2012; Ronevich *et al.*, 2012) and related issues are summarized in Suh (2014). It is known that adding less than 2 wt% of aluminium ameliorates the situation (Kim & Youn, 2008). A number of mechanisms have been proposed to explain the role of aluminium:

- It has been suggested that aluminium suppresses strain aging caused by carbon, thus reducing the flow stress and hence making hydrogen embrittlement less likely (Koyama *et al.*, 2013).

- The aluminium has been postulated to reduce the absorption of hydrogen (Chun *et al.*, 2012; Park *et al.*, 2012) but experimental observations contradict this - a variety of thermal desorption spectroscopy experiments suggest that the amount of hydrogen absorbed in the aluminium-containing steel is greater than in the alloys without aluminium (Han *et al.*, 2014; Ryu *et al.*, 2013), observations that are as yet unexplained.

- One interpretation builds on the effect of aluminium in increasing the stacking fault energy, thus reducing the possibility of transformation into ε-martensite or to twin, thereby mitigating hydrogen effects since twin and martensite interfaces feature at fracture surfaces (Ryu *et al.*, 2013).

- Another idea based on nanoindentation measurements is that the influence of hydrogen in reducing the shear modulus of the austenite contributes to embrittlement via the HELP mechanism; the presence of aluminium reduces the effect of hydrogen on the modulus and hence on the degree of embrittlement (Han *et al.*, 2014).

It is possible that all of these mechanisms actually play a role, but there recently has been an inspiring publication based on first principles calculations of binding energies in ferrite (Li *et al.*, 2013). That work indicated that aluminium-alloyed ferrite should be more resistant to hydrogen than silicon-alloyed ferrite. It was therefore decided to investigate whether similar calculations can reveal the possible role of aluminium in TWIP steels. As will be seen later, there are some fascinating outcomes which tally with previously unexplained experimental observations.

4.1.2   First-Principles Calculations

The calculations were performed using the Vienna Ab Initio Simulation Package (Kresse & Furthmüller, 1996a,b; Kresse & Hafner, 1993) within

the generalised gradient approximation of the Perdew-Burke-Ernzerhof (PBE) form (Perdew *et al.*, 1996) for electron exchange and correlation. The austenite was simulated using a $2 \times 2 \times 2$ supercell of the face-centred cubic (fcc) structure and calculations of the bulk properties were performed with a sufficiently high plane-wave cutoff energy, $400\,\text{eV}$. A hydrogen atom was added in both pure austenite, Fe_{32} and that containing Al, $Fe_{31}Al$. A $7 \times 7 \times 7$ k-point Monkhorst-Pack grid was used to sample the Brillouin zone. The first-order Methfessel-Paxton method (Methfessel & Paxton, 1989) was used for the Fermi-surface smearing in order to obtain accurate forces, with a smearing width of $0.1\,\text{eV}$. Both cell shape and atomic positions were permitted to relax for bulk calculations.

Austenite at ambient temperature is paramagnetic but its ground state has an antiferromagnetic double layer (AFMD) structure (Herper *et al.*, 1999). However AFMD is not consistent with the paramagnetic state and its relaxed lattice structure is tetragonal, $a = 3.54\,\text{Å}$, $c = 3.75\,\text{Å}$, (Acet *et al.*, 1994; Klaver *et al.*, 2012). For this reason, some studies select the ferromagnetic high-spin magnetic state of austenite which has a relaxed lattice parameter $a = 3.64\,\text{Å}$ (Jiang & Carter, 2003). Hydrogen-vacancy interactions in fcc iron have been investigated using both non-magnetic (NM) and AFMD states; there were differences in the energy values for the two states but the qualitative trends were independent of the magnetic state (Nazarov *et al.*, 2010). Others have considered only the NM state in the assessment of carbon (Abbasi *et al.*, 2011). Bearing these studies in mind, the non-magnetic state of austenite has been assumed in the present work.

The lattice parameter of austenite was calculated to be $3.44\,\text{Å}$, which compares well with the range of values in published work for NM austenite, 3.44-$3.45\,\text{Å}$(Jiang & Carter, 2003; Nazarov *et al.*, 2010). The reference state for hydrogen is the H_2 molecule, calculated by putting H_2 in a cubic box with $10\,\text{Å}$ sides and carrying out a Γ–point calculation. Its bond length was obtained to be $0.75\,\text{Å}$, consistent with (Nazarov *et al.*, 2010)

and the experimental value of $0.74\,\text{Å}$ (Huber & Herzberg, 1979). The lattice constant for $Fe_{31}Al$ was found to be $3.46\,\text{Å}$ which is $0.6\,\%$ larger than that of pure austenite.

The solution energy of hydrogen in Fe_{32} and $Fe_{31}Al$ can be studied to assess the interaction with aluminium with the hydrogen atoms located preferentially in the octahedral interstices (Nazarov *et al.*, 2010). For the Al containing system, $Fe_{31}Al$ was selected because the Al concentration is about $1.5\,\text{wt}\%$ which is consistent with the previously reported concentrations(Han *et al.*, 2014; Ryu *et al.*, 2013). There are 3 possible configurations with $Fe_{31}AlH$ as shown in Fig. 4.1.
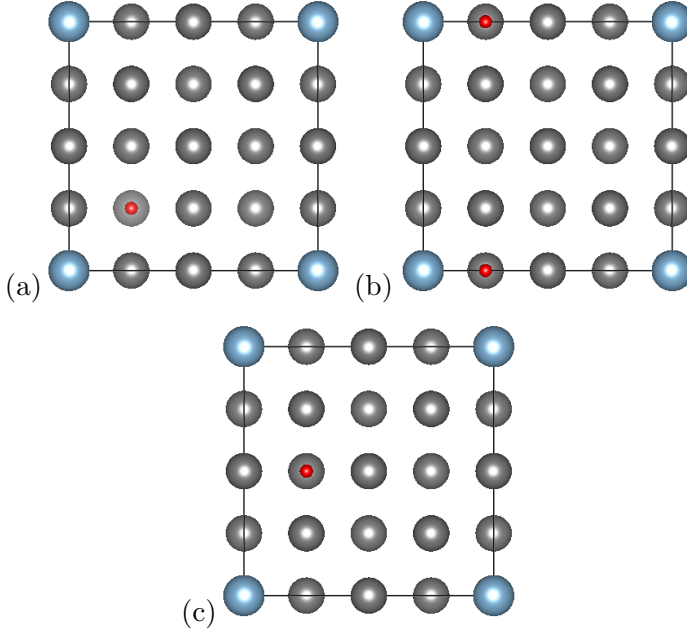
Figure 4.1: Atomic structures of $Fe_{31}AlH$, (a) oct1, (b) oct2, and (c) oct3. The grey, blue, and red spheres represent Fe, Al, and H atom, respectively. The cell contains 31 Fe atoms, 1 Al, and 1 H atom.

The most stable configuration was found to be oct1 from the calculation. Thus, all the following Al containing systems had the oct1

Table 4.1: Convergence tests results of the energy per atom in bulk Fe_{32}, $E_{atom}(Fe_{32})$, H_2 molecule, $E_{atom}(H_2)$, and the solution energy of $Fe_{32}H$, $E_s(Fe_{32}H)$ with varying cutoff energy, ENCUT.

ENCUT	200	300	400	500	error
$E_{atom}(Fe_{32})$, eV	-8.222	-8.153	-8.144	-8.144	0.000
$E_{atom}(H_2)$, eV	-3.323	-3.358	-3.376	-3.382	0.006
$E_s(Fe_{32}H)$, eV	0.211	0.061	0.072	0.060	0.011

configuration. The solution energies are defined as follows:

$$
\begin{aligned}
\Delta E_s(Fe_{32}H) &= E(Fe_{32}H) - E(Fe_{32}) - \frac{1}{2}E(H_2), \\
\Delta E_s(Fe_{31}AlH) &= E(Fe_{31}AlH) - E(Fe_{31}Al) - \frac{1}{2}E(H_2)
\end{aligned}
\tag{4.1}
$$

The obtained solution energies were 0.07 and $0.01\,\text{eV}$ for $Fe_{32}H$ and $Fe_{31}AlH$, respectively. The error in the solution enthalpy, $\pm0.01\,\text{eV}$, was calculated as the absolute difference between the default result (EN-CUT=$400\,\text{eV}$, N_k=7) and those with highest values of the varied input parameters. Tables 4.1 and 4.2 show the convergency test results with varying ENCUT and k-points, respectively. Thus, it was found that Al reduces the hydrogen solution energy. We can consider this energy difference as the binding energy of hydrogen near Al. Then, the binding energy of hydrogen near the Al atom is obtained to be $0.06\,\text{eV} \equiv 5.8\,\text{kJ}\,\text{mol}^{-1}$.

To understand why Al decreases the hydrogen solution energy, the distance between Al and the nearest Fe atoms was investigated. In pure iron, the distance between nearest atoms is $2.445\,\text{Å}$, and increases to $2.510\,\text{Å}$ in the aluminium-containing austenite along all directions. Fig. 4.2 shows the relaxed atomic structure for $Fe_{31}Al$. The blue and grey spheres represent Al and Fe atoms respectively. The red arrows mean the same distance, $2.510\,\text{Å}$. It is noteworthy that the distance between Fe atoms decreased even though the lattice parameter increased to $3.46\,\text{Å}$ due to

the repulsion around the Al atom. Since the most stable position of hydrogen is oct1, which has the largest space, it is possible to conclude that the reduction of hydrogen solution energy comes from the repulsion around the Al atom.

In addition, the effect of Mn was investigated with the $Fe_{27}Mn_5$ system considering the high Mn concentration of TWIP steels. Calculations were done using different configurations of Mn atoms and Fig. 4.3 shows the atomic structures of the $Fe_{26}Mn_5AlH$ system. The lattice parameters of $Fe_{27}Mn_5$ and $Fe_{26}Mn_5Al$ were found to be 3.45 and 3.46 Å. The hydrogen solution energies of $Fe_{27}Mn_5H$ and $Fe_{26}Mn_5AlH$ were found to be 0.045 and -0.019 eV respectively. In this case, the binding energy due to the Al atom can be obtained as $6.1\,kJ\,mol^{-1}$, which is almost the same as that of pure austenite. The solution energies and binding energies of Al are shown in Table 4.3.
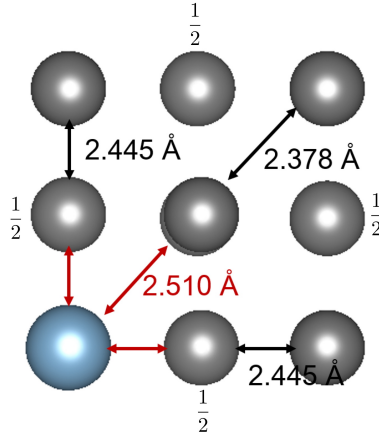
Figure 4.2: Atomic structure of $Fe_{31}Al$ with the distance between nearest atom. The red arrows indicate the same distance between Al and Fe atom. The fractions indicate the height of the atom in the direction normal to the diagram; unlabelled atoms are at heights 0,1.
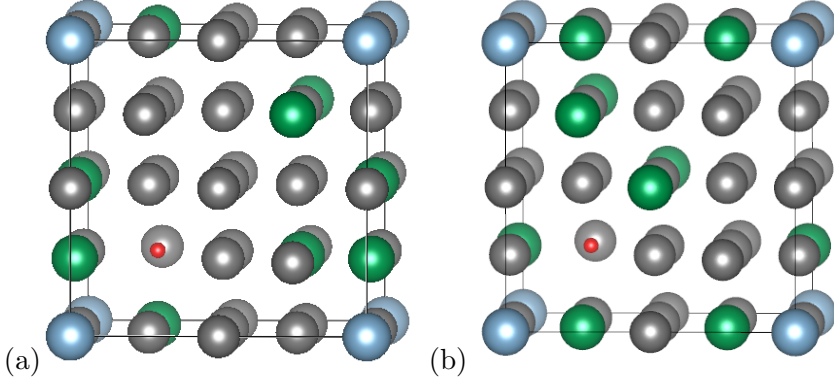
Figure 4.3: Atomic structures of $Fe_{26}Mn_5AlH$. The grey, green, blue and red spheres are Fe, Mn, Al and H atoms. Mn atoms were randomly added.

Table 4.2: Convergence tests results of the energy per atom in bulk Fe_{32}, $E_{atom}(Fe_{32})$, and the solution energy of $Fe_{32}H$, $E_s(Fe_{32}H)$ with varying number of k-point, N_k.

N_k	5	7	9	error
$E_{atom}(Fe_{32})$, eV	-8.144	-8.144	-8.144	0.000
$E_s(Fe_{32}H)$, eV	0.087	0.072	0.077	0.005

Table 4.3: The hydrogen solution energies and the binding energies of Al from first-principles calculations.

	$Fe_{32}H$	$Fe_{31}AlH$	$Fe_{27}Mn_5H$	$Fe_{26}Mn_5AlH(1)$	$Fe_{26}Mn_5AlH(2)$
E_s, eV	0.07	0.01	0.04	-0.02	-0.02
E_b, eV	-	0.06	-	0.06	0.06

4.1.3   Modelling of Hydrogen Desorption

A trap is defined as a location within the lattice where a hydrogen atom can enter a potential well that is deeper than in the perfect lattice. The first principles calculations indicate that the Al atom is such a trap; there are 8 possible positions for hydrogen in this supercell. If it is assumed that only half of those sites can be occupied at any instant due to repulsion between adjacent hydrogen atoms, then the trap density is $4/(2 \times 3.46\,\text{\AA})^3 \equiv 1.21 \times 10^{28}\,\text{m}^{-3}$. The hydrogen occupancy of these traps should be much less than 1, enabling the use of some standard theory for the apparent diffusivity D as follows (Oriani, 1970):

$$D = \frac{D_L}{1 + \frac{N_t}{N_l} \exp\left(\frac{E_b}{RT}\right)} \tag{4.2}$$

where D_L is the hydrogen diffusivity in the austenite lattice in the absence of traps, N_l and N_t are the densities of lattice and trap sites, respectively, R is the gas constant, T is the absolute temperature, and E_b is the binding energy. Furthermore, the amount of trapped hydrogen is given by:

$$C_t = C_l \frac{N_t}{N_l} \exp\left(\frac{E_b}{RT}\right) \tag{4.3}$$

where C_l and C_t are concentrations of hydrogen at lattice and trap sites. Fig. 4.4a compares the hydrogen diffusivity in austenite 304L stainless steel (Xiukui *et al.*, 1989) to the lower diffusivity obtained for the Al containing austenite. To the best of our knowledge, there is no report about the direct observation of the diffusivity of hydrogen in pure austenite or TWIP steels. It is emphasised that the reduction of diffusivity is due solely to the aluminium atoms acting as weak traps, and not due to any changes in the local atomic arrangements around the aluminium atom. Fig. 4.4b shows the ratio of C_t/C_l calculated using equation 4.3. Even though the Al-H binding energy is relatively small, it can increase the to-

tal amount of absorbed hydrogen almost 2.3 times at room temperature. In practice, the degree of increase should be less than 2.3 because the effects of other trap sites such as dislocations or grain boundaries were not accounted for. Besides, the measured hydrogen amount depends on the penetration depth, which may differ from austenite to Al-containing austenite due to the different diffusivities. Indeed, it has been reported that the addition of Al increased the total amount of absorbed hydrogen by 20 % (Han *et al.*, 2014; Ryu *et al.*, 2013).

The effect of Al addition on hydrogen thermal desorption with the obtained trap density and binding energy have been simulated as reported in detail in this chapter. This simulation involves the lattice hydrogen diffusion and trapping or detrapping behaviour based on the local equilibrium assumption of Oriani (1970). The thermal desorption rates of austenite and Al-containing austenite were simulated assuming the following conditions: thickness 1 mm, heating rate $100\,^{\circ}\mathrm{C}\,\mathrm{h}^{-1}$, charging time 72 h, and room temperature releasing time 30 min. The diffusivity was obtained from Xiukui *et al.* (1989), and the surface hydrogen concentration was 23 ppmw, as reported by Ryu *et al.* (2013). This value for lattice diffusivity D_L is used for both simulations, but when aluminium atoms are present, they act as traps and therefore the overall diffusivity in the simulation becomes D. The trap density and binding energy were obtained as discussed earlier in this chapter. The predicted results are shown alongside published data (Han *et al.*, 2014; Ryu *et al.*, 2013) in Fig. 4.5. The original measurements (Han *et al.*, 2014; Ryu *et al.*, 2013) monitored temperatures via the furnace controller; therefore calibration experiments were conducted by attaching a thermocouple to the sample itself, and relating the directly measured temperature to that output by the TDA equipment. The plots in Fig. 4.5 are therefore corrected relative to the originals. The specimen thickness is identical for all those results but the charging time of Han *et al.* (2014) is 48 h while the simulation and Ryu *et al.* (2013) used 72 h. No significant change in the peak tem-
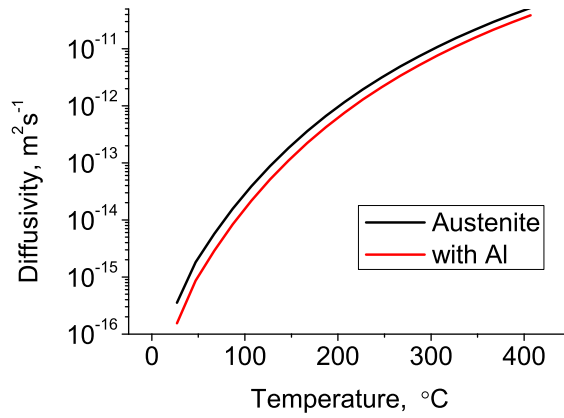
(a)
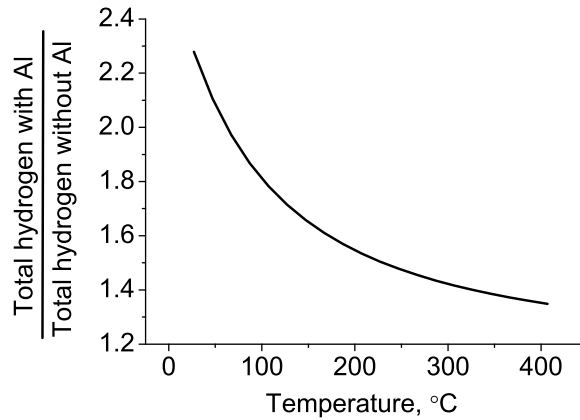
(b)

Figure 4.4: The trap effect of Al on (a) hydrogen diffusivity and (b) concentration. The black and red solid lines indicate the diffusivity of hydrogen in austenite and Al containing austenite, respectively.

67

perature with the addition of Al was predicted, but the peak height and total amount of hydrogen increased. These predictions coincide with the experimental observations.

4.2 Numerical Analysis of Hydrogen Desorption in Austenite

4.2.1 Introduction

In chapter 3, the new method to predict the TDS curves was introduced and applied to the ferrite. For example, it was found that a stronger binding energy shifts the peak to higher temperatures and that a larger trap density increases the peak height. In this chapter, the same method is applied to the austenite. For the simulation, the diffusivity from the published data, $D_0 = 4.79 \times 10^{-7}\,\mathrm{m^2\,s^{-1}}$, $E_d = 51.6\,\mathrm{kJ\,mol^{-1}}$ (Xiukui *et al.*, 1989) is used and the number of elements per mm was increased to 1600 due to the slow diffusivity.

Hydrogen desorption in austenite is more complex because its diffusivity is much slower and it is very difficult to saturate the sample at room temperature. The trap binding energy in austenite has not been explored quantitatively except very few studies (Ningshen *et al.*, 2001; Park *et al.*, 2002; So *et al.*, 2009). Ningshen *et al.* reported two detrapping activation energies, 27 and 41 kJ mol^{-1} which correspond to nitrogen-hydrogen binding and interstital hydrogen, respectively. Park *et al.* also reported the detrapping activation energy of dislocation, retained austenite and TiC interface to be 26, 55, and 87 kJ mol^{-1}, respectively. So *et al.* reported the TDS peaks from grain boundaries and dislocations overlapped, with both having a same detrapping activation energy of 35 kJ mol^{-1}; an additional desorption peak from mechanical twin boundaries at higher temperature was reported with a detrapping activation energy of 62 kJ mol^{-1}. However, this additional peak was not observed in other literature (Koyama
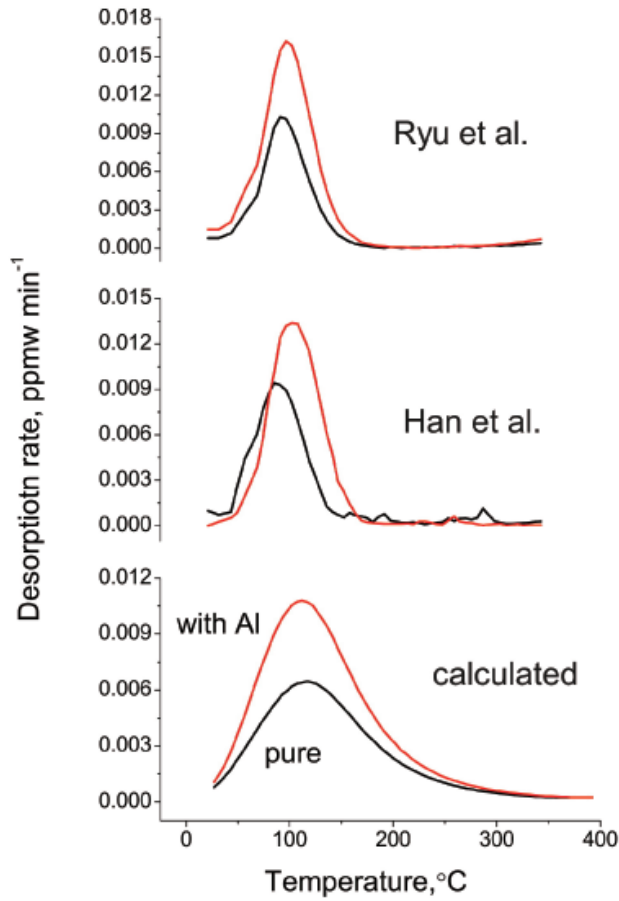
Figure 4.5: The reported and predicted hydrogen thermal desorption rate of austenite and Al containing austenite with the calculated trap density and binding energy. The figures are reproduced from (Han *et al.*, 2014; Ryu *et al.*, 2013) and the bottom figure is obtained by simulation.

4.2. Numerical Analysis of Hydrogen Desorption in Austenite

et al., 2013; Ryu *et al.*, 2013).

All of the literature has used the Kissinger's method so the data should be re-analyzed given that the Kissinger's method assumes the rate controlling step as a detrapping process and does not consider diffusion. Moreover, the detrapping activation energy is the sum of diffusion activation energy and trap binding energy and diffusion activation energy in austenite is about 48-54 kJ mol^{-1}(Xiukui *et al.*, 1989) which indicates that some binding energies of the reported detrapping activation energies are negative.

4.2.2 Parameter Sensitivity

The reference conditions are sample thickness 1 mm, charging time 72 h, binding energy 30 kJ mol^{-1}, trap density $3{\times}10^{24}\,\text{m}^{-3}$, heating rate $100\,^{\circ}\text{C h}^{-1}$ room temperature aging time of 45 min, and lattice hydrogen concentration at the surface of 1 ppmw.

The effects of trap binding energy are first investigated. The binding energies were varied from 30 to 60 kJ mol^{-1} and the predicted TDS curves are shown in Fig. 4.6. Also the total hydrogen concentration with the time with the sample without trapping and the sample with varying binding energy are shown in Fig. 4.8. The dashed line indicates the temperature with given heating rate. Since the diffusivity of hydrogen in austenite is slow, the sample is not saturated even after 72 h of charging as shown in Fig. 4.7. The hydrogen penetrates to about 0.05 mm without trapping and the penetration depth was reduced to 0.02 mm for the samples with traps. The depth also decreases as the binding energy increases from 30 to 60 kJ mol^{-1}. Note that the simulation is for half of sample thickness 0.5 mm and $x = 0.0$ in the graph indicates the sample surface.

When results of the sample without trap and the sample which trap binding energy is 30 kJ mol^{-1} are compared, the peak temperature is relatively insensitive to the presence or absence of traps because the controlling activation energy is that for diffusion, which is greater than the
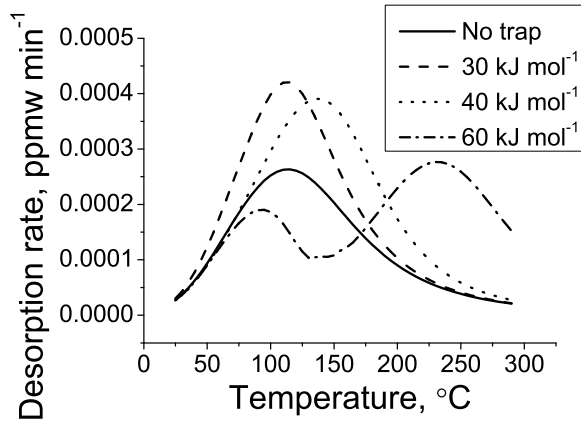
Figure 4.6: Predicted TDS curves with different binding energies.
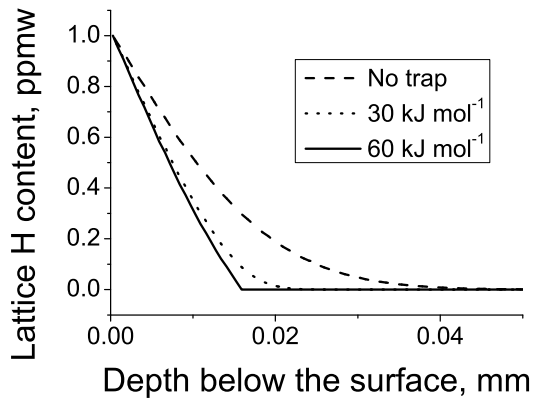
Figure 4.7: The lattice hydrogen profile after charging samples with different binding energies.

71

binding energy of the trap. However, the peak height is greater for the sample containing the traps because the total amount of hydrogen that can be absorbed into a sample with defects is naturally larger. From Fig. 4.8a, it can be confirmed that the lattice hydrogen starts to decrease after heating starts in the case of sample without traps. In the case of the sample with the binding energy of $30 \, \text{kJ} \, \text{mol}^{-1}$, as heating starts, trapped hydrogen starts to escape from the traps which causes a slight increase in the lattice hydrogen amount, Fig. 4.8b.

As the trap binding energy increases, the peak shifts to higher temperatures. As the binding energy is stronger than the diffusion activation energy, the peak splits into two parts. The lattice hydrogen starts to decrease after heating starts because trapped hydrogen remains at that trap sites due to the strong binding energy, Fig. 4.8c. The peak at low temperature is from the lattice hydrogen, and the peak at higher temperature is from the trapped hydrogen. What is interesting is that the amount of trapped hydrogen slightly increases during heating and the reason can be explained from Fig. 4.9c.

Fig. 4.9 shows the free and trapped hydrogen profile in the sample after charging, after aging and during heating. For the results during heating, the temperature was chosen to be $100 \, °\text{C}$ so that some hydrogen remains in the sample. The profile change of lattice hydrogen is similar for all those samples even though the penetration depth is different. On the other hands, the trapped hydrogen profiles of the sample with binding energy $30 \, \text{kJ} \, \text{mol}^{-1}$ and $60 \, \text{kJ} \, \text{mol}^{-1}$ shows differences. For both cases, the trapped hydrogen profile after aging coincides with the profile after charging although the trap with binding energy $60 \, \text{kJ} \, \text{mol}^{-1}$ is saturated near the sample surface and the less potent traps are not saturated. However, the trapped hydrogen profile at $100 \, °\text{C}$ shows different behavior. In the case of the trap with binding energy $30 \, \text{kJ} \, \text{mol}^{-1}$, the amount of trapped hydrogen reduced significantly simply because it is less potent trap. On the other hand, the trapped hydrogen with binding energy
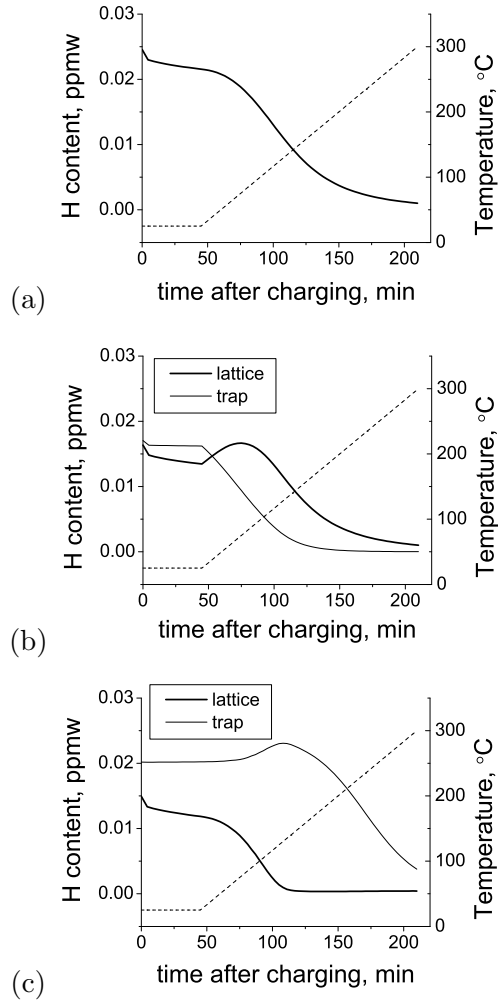
Figure 4.8: The total H content as a function of time after charging of (a) a sample without trapping, (b) sample with trap which binding energy $30\,\mathrm{kJ\,mol^{-1}}$, and (c) sample with trap which binding energy $60\,\mathrm{kJ\,mol^{-1}}$. The dashed line indicates the temperature and the vertical scale on the right hand side refers to temperature and that on the left to hydrogen amounts.

(a)

(b)

(c)
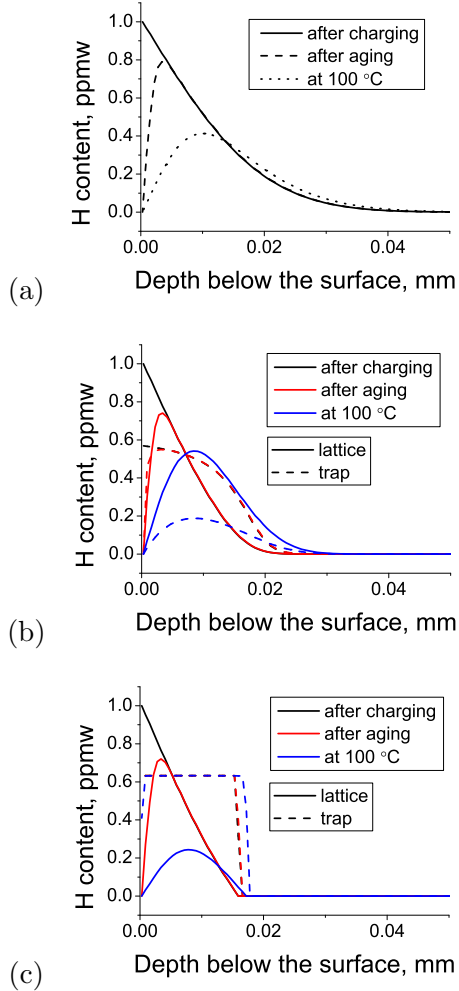
Figure 4.9: The hydrogen profile in the sample inside after charging, after aging and during heating. For the results during heating, the temperature was chosen to be $100\,°C$; (a) a sample without trapping, (b) sample with trap which binding energy $30\,\text{kJ}\,\text{mol}^{-1}$, and (c) sample with trap which binding energy $60\,\text{kJ}\,\text{mol}^{-1}$. The solid lines indicate the lattice hydrogen profile and dashed lines indicate the trapped hydrogen profile.

$60\,\text{kJ}\,\text{mol}^{-1}$ still remains and even its penetration depth was increased. This is because the lattice hydrogen diffuses inside the sample where hydrogen was not saturated, and from the local equilibrium condition, some hydrogen is trapped with binding energy $60\,\text{kJ}\,\text{mol}^{-1}$ *i.e.*, some hydrogen escaped from lattice becomes re-trapped by the traps with binding energy $60\,\text{kJ}\,\text{mol}^{-1}$.
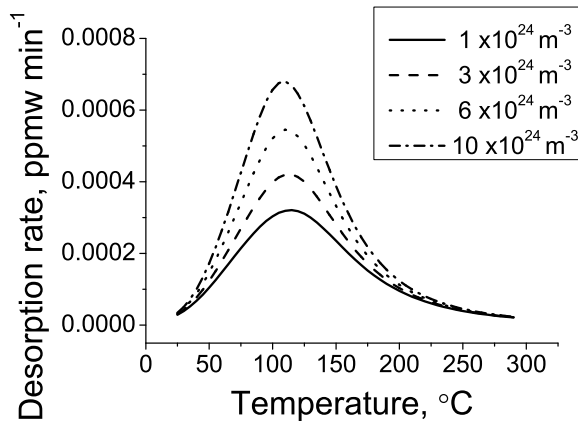
Figure 4.10: Predicted TDS curves with different trap densities.

Second, the effects of trap density are investigated. The binding energy was varied from 10^{24} to $10^{25}\,\text{m}^{-3}$ with the reference condition which was described in the first paragraph of chapter 4.2.2 and the predicted TDS curves are shown in Fig. 4.10. As trap density increases, the peak height increases and no difference in the peak temperature is obtained. The lattice and trapped hydrogen profiles after charging with different trap densities are shown in Fig. 4.11. The amount of trapped hydrogen increases as the trap density increase, and the hydrogen penetration depth decreases as the trap density increases.

Even though the trap density $10^{25}\,\text{m}^{-3}$ was larger than the trap density of the ferrite in chapter 3, the desorption rate is much lower than the reported value. For example, the maximum desorption rate of the 0% pre-
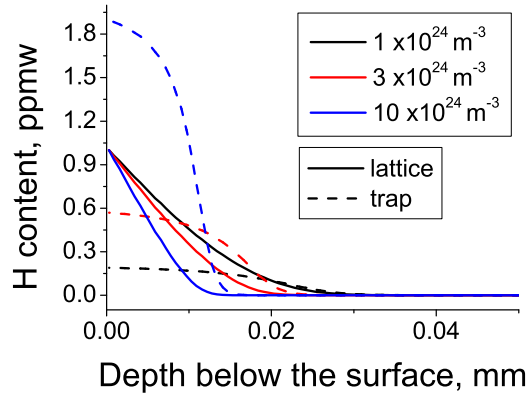
Figure 4.11: The lattice and trapped hydrogen profile after charging with different trap densities.

strained TWIP steel after $72\,\mathrm{h}$ of charging was about $0.01\,\mathrm{ppmw\,min^{-1}}$ (Ryu *et al.*, 2013). Thus, the effects of lattice hydrogen concentration at the surface was investigated. The lattice hydrogen concentration after hydrogen charging was evaluated to be 18-23 ppmw with different current densities (Ryu *et al.*, 2013). The predicted TDS curves with different hydrogen concentrations are shown in Fig. 4.12. The values were varied from 1 to 30 ppmw. As the surface concentration increases, so does peak height. The lattice and trapped hydrogen profiles after charging with different surface concentrations are shown in Fig. 4.13. In the case of surface concentration 10 and 30 ppmw, the trapped hydrogen content at the surface is the same which indicates the traps are saturated. No effects of surface concentration on the TDS curves was predicted in the ferrite when the sample was saturated; however, in the case of austenite an increase in the desorption rate is observed. This is mainly from the increase in lattice hydrogen but it can also be found from the hydrogen penetration depth. Even though the trap is saturated at the surface, the hydrogen penetration depth is longer as surface concentration increases, resulting in the total hydrogen desorption increase.
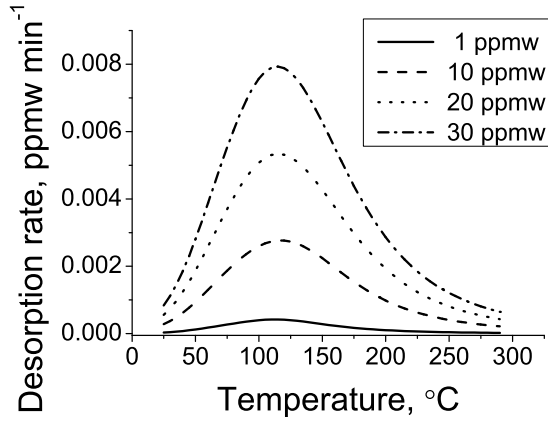
Figure 4.12: Predicted TDS curves with different surface concentrations.
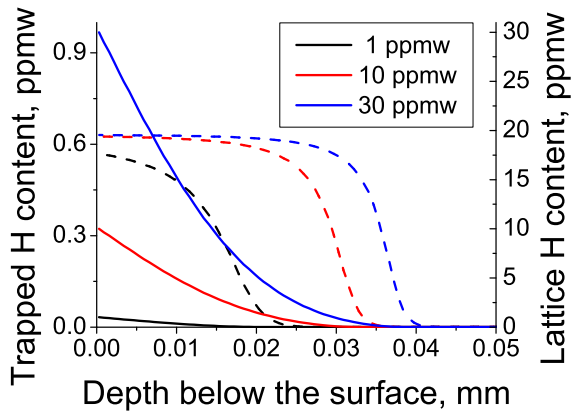
Figure 4.13: The lattice and trapped hydrogen profile after charging with different surface concentration. The solid and dashed lines indicate the profile of lattice and trapped hydrogen. The vertical scale on the right hand side refers to lattice hydrogen content and that on the left to trapped hydrogen content.

4.2. Numerical Analysis of Hydrogen Desorption in Austenite
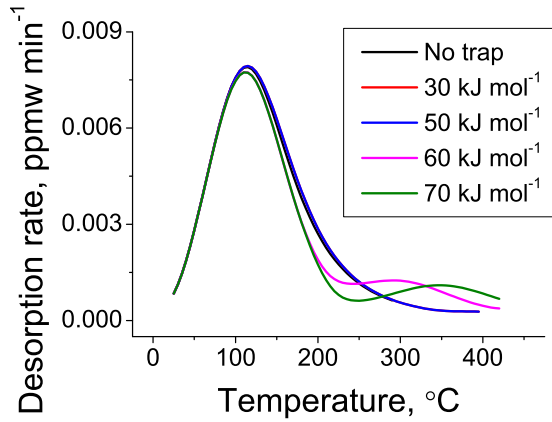
Figure 4.14: The predicted TDS curves with different binding energies.

The effects of binding energy were investigated again with an increased surface concentration of 30 ppmw. All the other conditions are the same with the reference condition which was given in the first paragraph of this chapter 4.2.2. The binding energy was varied from 30 to $70\,\mathrm{kJ\,mol^{-1}}$ and the results are shown in Fig. 4.14. Unlike results indicated in the Fig. 4.6, there is no change in the desorption curve from the sample without traps and that with $E_b < 50\,\mathrm{kJ\,mol^{-1}}$. The desorption peak splits for $E_b > 50\,\mathrm{kJ\,mol^{-1}}$, Fig. 4.6. The total hydrogen contents as a function of time after charging are shown in Fig. 4.15. The amounts of lattice hydrogen are much larger than Fig. 4.6, due to the high surface concentration. Also, the contribution of trapped hydrogen is small relative to that of the lattice. In the case of the sample $E_b = 30\,\mathrm{kJ\,mol^{-1}}$, the trapped hydrogen amount decreases as heating starts, but the effect is not shown in the desorption curve simply because the amount is relatively small compared with the lattice hydrogen. However, in the case of the sample when E_b exceeds the diffusion activation energy, the lattice hydrogen starts to be re-trapped by the trap sites at high temperature resulting in the desorption peak at elevated temperatures.

(a)

(b)

(c)
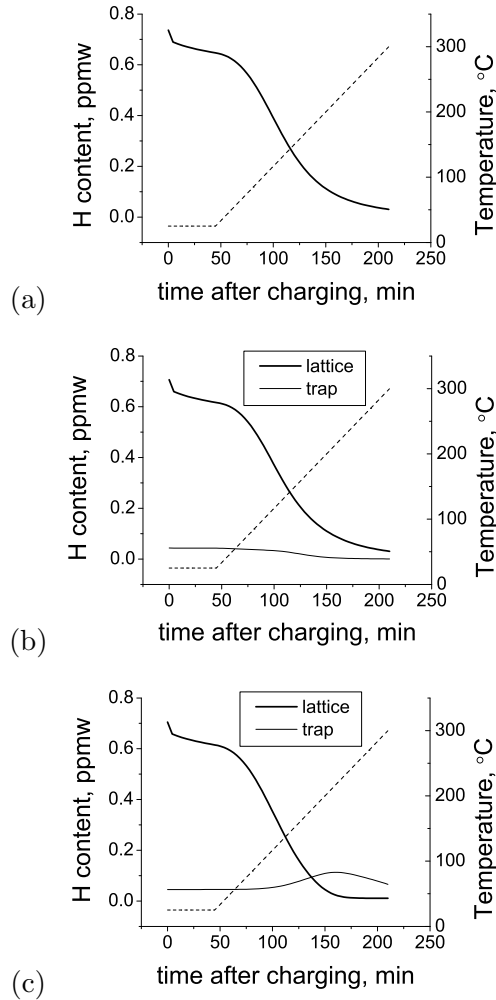
Figure 4.15: The total H content as a function of time after charging of (a) a sample without trapping, (b) sample with trap which binding energy $30\,\mathrm{kJ\,mol^{-1}}$, and (c) sample with trap which binding energy $60\,\mathrm{kJ\,mol^{-1}}$. The dashed line indicates the temperature and the vertical scale on the right hand side refers to temperature and that on the left to hydrogen amounts. The surface concentration is $30\,\mathrm{ppmw}$.
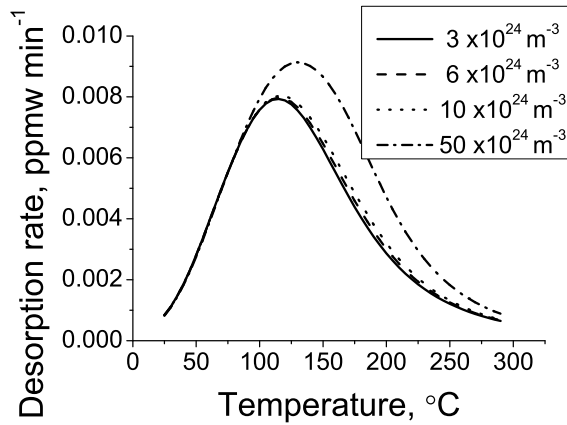
Figure 4.16: The predicted TDS curves with different binding energy.

The effects of trap density are investigated again with the increased surface concentration, 30 ppmw. All the other conditions are identical with the reference condition which is given in the first paragraph of this chapter 4.2.2 and the results are shown in Fig. 4.16. The effects of trap density less than was $10^{25}\,\text{m}^{-3}$ was negligible.

4.2.3 Application to Literature Data

There are published TDS data for different grain sizes in Fe-0.6C-18Mn wt% steel (Ryu *et al.*, 2013; So *et al.*, 2009). The desorption peak height increased as the grain size decreased or the pre-strain increased. Numerical analysis method is applied to the published data (Ryu *et al.*, 2013) after calibrating the temperature profile. The temperature profile was modified by measuring the temperature of the sample during heating. The TDS data of sample with grain size $\bar{L}$ 2.3, 5.2, 8.4 µm were analyzed. The grain sizes were obtained by using the lineal intercepts method.

The trap binding energy and density were obtained from the measured data of the sample of which grain size is 8.4 µm and then, the trap density for the samples with different grain sizes were calculated by assuming it
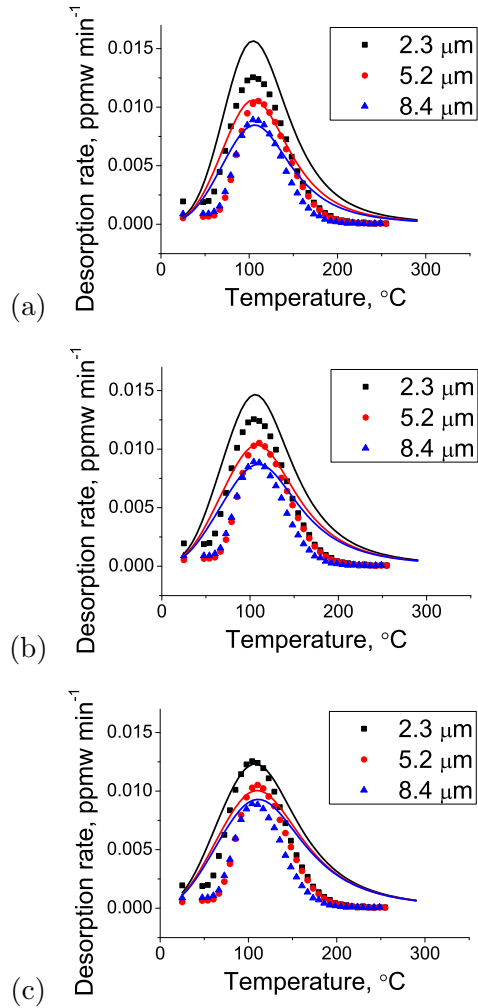
Figure 4.17: Measured TDS data and predicted curves(solid lines) with the surface concentration (a) 10, (b) 20, and (c) 30 ppmw. The measured data are reproduced from Ryu *et al.* (2013).

Table 4.4: The binding energies ($kJ\,mol^{-1}$) and trap densities ($10^{25}\,m^{-3}$) for the samples with different grain size (μm)

Surface concentration	Grain size	Binding energy	Trap density
10 ppmw	2.3	22	82.60
	5.2	22	36.54
	8.4	22	22.60
20 ppmw	2.3	19	41.74
	5.2	19	18.46
	8.4	19	11.42
30 ppmw	2.3	15	30.43
	5.2	15	13.46
	8.4	15	8.33

to be proportional to the grain surface area. The grain surface area per unit volume S_V was calculated by equation 4.1.

$$S_V = 2\bar{L}^{-1} \tag{4.4}$$

Then, using the obtained binding energy and trap density, the TDS curves were predicted and the results are shown in Fig. 4.17 and for the parameters in Table 4.4. The surface concentration was varied because it determines the contribution of the lattice hydrogen. After fixing the lattice hydrogen contribution, the change in the TDS curves as a function of grain size was ascribed to the trap density difference. The best fitting result was obtained when the surface concentration is set at 30 ppmw and all the measured data were well reproduced with binding energy $15\,kJ\,mol^{-1}$. When the surface concentration is less than 30 ppmw, the contribution of the lattice hydrogen was too small, *i.e.*, the contribution of the trapped hydrogen was exaggerated resulting in an overestimation of the data for the 2.3 μm grain size sample. The hydrogen contents as a function of time after charing are shown in Fig. 4.18. The trapped hydrogen concentration

4.2. Numerical Analysis of Hydrogen Desorption in Austenite

at the surface increases with the trap density and as heating starts, the trapped hydrogen escapes from grain boundaries resulting in the lattice hydrogen concentration increase. The concentration of trapped hydrogen becomes almost 0 after 150 min from the charging, *i.e.*, the temperature is above 200 °C, while some lattice hydrogen still remains in the sample at that temperature. The free and trapped hydrogen profiles after charging are shown in Fig. 4.19. The hydrogen penetration depth is about 0.02-0.04 μm and it decreases as the grain size increases.

It was found that grain boundaries in austenite are less potent traps than those in ferrite. The value is similar with the reported value $18\,\mathrm{kJ\,mol}^{-1}$ for the dislocation trapping in austenitic stainless steels (West & Louthan, 1979) and the similar tenancy was reported from first-principles study (Du *et al.*, 2011). They calculated the hydrogen solution energies of the coherent $\Sigma 3[1\bar{1}0](112)$ ferrite and $\Sigma 3[1\bar{1}0](111)$ austenite grain boundaries and the less coherent $\Sigma 5[001](310)$ ferrite and $\Sigma 11[1\bar{1}0](113)$ austenite grain boundaries. By comparing the solution energies of grain boundaries and that of bulk, the binding energies were obtained. In all cases, the grain boundary binding energy for austenite was much less than the that of ferrite. The authors found that the volumes of interstitial sites in austenite at those grain boundaries are almost bulk-like and this causes weaker binding energies than those of ferrite.

In addition, the trap densities for those simulated curves were much larger than those of ferrite. This is because the sample is not saturated although the hydrogen concentration was calculated on the basis of the entire sample. If the effective part of the sample is considered, then the trapped hydrogen concentration should be much greater. In order to explain such high concentration, larger trap densities were needed to reproduce the measured data.

In this model, the pipe diffusion of hydrogen is not considered. However, it may be important, given that diffusion diffusion through the perfect lattice is difficult, and the obtained trap densities are much greater

(a)

(b)

(c)
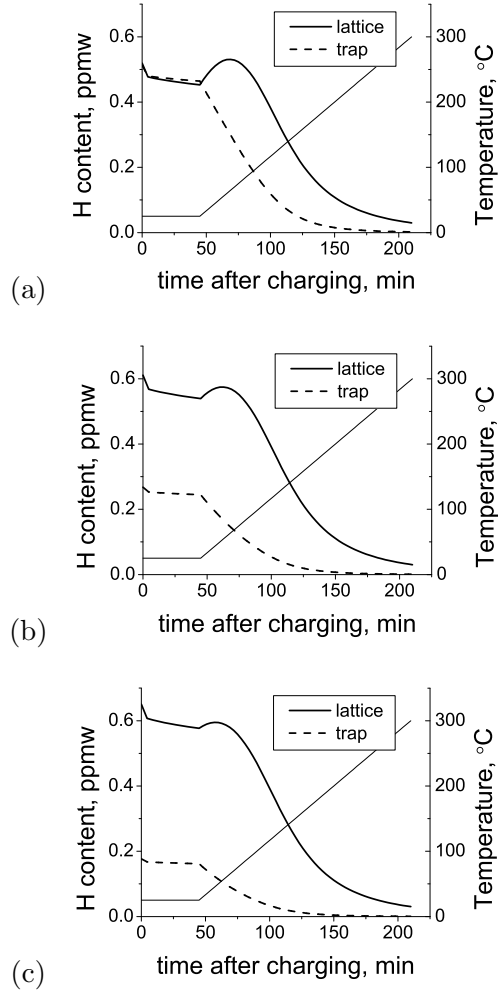
Figure 4.18: The H content as a function of time after charging of the samples with (a) $\bar{L} = 2.3\,\mu$m, (b) $\bar{L} = 5.2\,\mu$m, and (c) $\bar{L} = 8.4\,\mu$m. The dashed line indicates the temperature and the vertical scale on the right hand side refers to temperature and that on the left to hydrogen amounts.

(a)

(b)

(c)
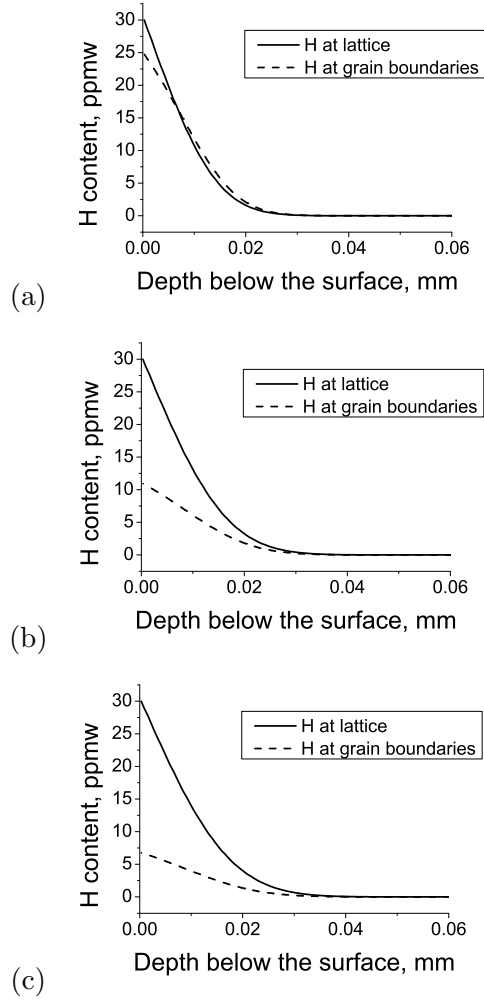
Figure 4.19: The hydrogen profile in the sample inside after charging of the samples with (a) $\bar{L} = 2.3\,\mu$m, (b) $\bar{L} = 5.2\,\mu$m, and (c) $\bar{L} = 8.4\,\mu$m.

than in the ferrite. However, the effect of pipe diffusion in austenite is not clear in the literature. In deformed austenitic stainless steel, the diffusivity increases with plastic strain (Tsong-Pyng & Altstetter, 1986) however, the reason is ascribed to α' martensite formation.

4.3 Summary

It is found that aluminium atoms in TWIP steel cause a localised dilation that better accommodates hydrogen, a phenomenon expressed via an Al-H binding energy. This binding energy when implemented in trapping theory indicates both that the presence of aluminium allows the TWIP steel to absorb more hydrogen than a corresponding steel that is aluminium-free, and that the diffusion coefficient for hydrogen is significantly affected by the presence of aluminium.

The numerical analysis method was applied to the austenite. The TDS analysis of austenite is more complex than ferrite because the sample is not saturated at room temperature and because the rate determining step is not only the detrapping process. The effects of binding energy, trap density, and the surface concentration were investigated and the published experimental data were analyzed. The binding energy of grain boundaries in TWIP steel was evaluated to be $15\,\mathrm{kJ\,mol^{-1}}$ when the surface concentration was $30\,\mathrm{ppmw}$. The trap density should be much higher than the ferrite case, because the sample is unsaturated. The physical meaning of trap density needs to be studied more.

References

Abbasi, A., Dick, A., Hickel, T. & Neugebauer, J. (2011). First-principles investigation of the effect of carbon on the stacking fault energy of Fe-C alloys. *Acta Materialia*, **59**, 3041–3048. 60

ACET, M., ZÄHRES, H., WASSERMANN, E.F. & PEPPERHOFF, W. (1994). High-temperature moment-volume instability and anti-invar of γ-Fe. *Physical Review B*, **49**, 6012–6017. 60

BOUAZIZ, O., ALLAIN, O.S. & SCOTT, C. (2008). Effect of grain and twin boundaries on the hardening mechanisms of twinning-induced plasticity steels. *Scripta Materialia*, **58**, 484–487. 58

CHIN, K.G., KANG, C.Y., SHIN, S.Y., HONG, S.K., LEE, S.H., KIM, H.S., KIM, K.H. & KIM, N.J. (2011). Effects of Al addition on deformation and fracture mechanisms in two high manganese TWIP steels. *Materials Science and Engineering A*, **528**, 2922–2928. 58

CHUN, Y., PARK, K. & LEE, C. (2012). Delayed static failure of twinning-induced plasticity steels. *Scripta Mater*, **66**, 960–965. 59

DU, Y.a., ISMER, L., ROGAL, J., HICKEL, T., NEUGEBAUER, J. & DRAUTZ, R. (2011). First-principles study on the interaction of H interstitials with grain boundaries in α- and γ-Fe. *Phys. Rev. B*, **84**, 144121. 83

FROMMEYER, G., BRÜX, U. & NEUMANN, P. (2003). Supra-ductile and high-strength manganese–TRIP/TWIP steels for high energy absorption purposes. *ISIJ International*, **43**, 438–446. 58

HAN, D.K., KIM, Y.M., HAN, H.N., BHADESHIA, H. & SUH, D.W. (2014). Hydrogen and aluminium in high-manganese twinning-induced plasticity steel. *Scripta Materialia*, **80**, 9–12. vi, 59, 61, 66, 69

HERPER, H.C., HOFFMANN, E. & ENTEL, P. (1999). Ab initio full-potential study of the structural and magnetic phase stability of iron. *Physical Review B*, **60**, 3839–3848. 60

HUBER, K.P. & HERZBERG, G. (1979). *Constants of diatomic molecules*. Springer. 61

JIANG, D.E. & CARTER, E.A. (2003). Carbon dissolution and diffusion in ferrite and austenite from first principles. *Physical Review B*, **67**, 214103. 60

KIM, H.J. & YOUN, S.K. (2008). Three dimensional analysis of high frequency induction welding of steel pipes with impeder. *Journal of Manufacturing Science and Engineering, Transactions of the ASME*, **130**, 0310051–0310057. 58

KLAVER, T.P.C., HEPBURN, D.J. & ACKLAND, G.J. (2012). Defect and solute properties in dilute Fe-Cr-Ni austenitic alloys from first principles. *Physical Review B*, **85**, 174111. 60

KOYAMA, M., AKIYAMA, E., SAWAGUCHI, T., RAABE, D. & TSUZAKI, K. (2012). Hydrogen-induced cracking at grain and twin boundaries in an Fe-Mn-C austenitic steel. *Scripta Materialia*, **66**, 459–462. 58

KOYAMA, M., AKIYAMA, E. & TSUZAK, K. (2013). Effects of static and dynamic strain aging on hydrogen embrittlement in TWIP steels containing Al. *ISIJ international*, **53**, 1268–1274. 58, 68

KRESSE, G. & FURTHMÜLLER, J. (1996a). Efficiency of ab-initio total energy calculations for metals and semiconductors using a plane wave basis set. *Computational Materials Science*, **6**, 15–50. 59

KRESSE, G. & FURTHMÜLLER, J. (1996b). Efficient iterative schemes for ab initio total-energy calculations using a plane wave basis set. *Physical Review B*, **54**, 11169. 59

KRESSE, G. & HAFNER, J. (1993). Ab initio molecular dynamics for open-shell transition metals. *Physical Review B*, **48**, 13115. 59

LI, Y., CHEN, C. & ZHANG, F. (2013). Al and Si influences on hydrogen embrittlement of carbide-free bainitic steel. *Advances in Materials Science and Engineering*, **2013**, 382060. 59

88

METHFESSEL, M.P.A.T. & PAXTON, A.T. (1989). High-precision sampling for brillouin-zone integration in metals. *Physical Review B*, **40**, 3616–3621. 60

NAZAROV, R., HICKEL, T. & NEUGEBAUER, J. (2010). First-principles study of the thermodynamics of hydrogen-vacancy interaction in fcc iron. *Physical Review B*, **82**, 224104. 60, 61

NINGSHEN, S., UHLEMANN, M., SCHNEIDER, F. & KHATAK, H. (2001). Diffusion behaviour of hydrogen in nitrogen containing austenitic alloys. *Corrosion Science*, **43**. 68

ORIANI, R.A. (1970). The diffusion and trapping of hydrogen in steel. *Acta Metallurgica*, **18**, 147–157. 65, 66

PARK, I.J., JEONG, K.H., JUNG, J.G., LEE, C.S. & LEE, Y.K. (2012). The mechanism of enhanced resistance to the hydrogen delayed fracture in al-added fe–18mn–0.6 c twinning-induced plasticity steels. *international journal of hydrogen energy*, **37**, 9925–9932. 59

PARK, Y., MAROEF, I., LANDAU, A. & OLSON, D. (2002). Retained austenite as a hydrogen trap in steel welds. *Weld. Journal-New York-*. 68

PERDEW, J.P., BURKE, K. & ERNZERHOF, M. (1996). Generalized gradient approximation made simple. *Physical Review Letters*, **77**, 3865–3868. 60

REMY, L. & PINEAU, A. (1977). Twinning and strain-induced F.C.C.→H.C.P. transformation in the Fe-Mn-Cr-C system. *Materials Science and Engineering*, **28**, 99–107. 58

RONEVICH, J.A., KIM, S.K., SPEER, J.G. & MATLOCK, D.K. (2012). Hydrogen effects on cathodically charged twinning–induced plasticity steel. *Scripta Materialia*, **66**, 956–959. 58

RYU, J.H., KIM, S.K., LEE, C.S., SUH, D.W. & BHADESHIA, H. (2013). Effect of aluminium on hydrogen-induced fracture behaviour in austenitic FeMnC steel. *Proc. R. Soc. A Math. Phys. Eng. Sci.*, **469**. vi, viii, 59, 61, 66, 69, 70, 76, 80, 81

SO, K., KIM, J., CHUN, Y., PARK, K., LEE, Y. & LEE, C. (2009). Hydrogen delayed fracture properties and internal hydrogen behavior of a Fe-18Mn-1.5 Al-0.6C TWIP steel. *ISIJ international*, **49**, 1952–1959. 68, 80

SUH, D.W. (2014). Critical assessment: Hydrogen-induced fracture in austenitic, high-manganese TWIP steel. *Materials Science and Technology*. 58

TSONG-PYNG, P. & ALTSTETTER, C. (1986). Effects of deformation on hydrogen permeation in austenitic stainless steels. *Acta Metall.*, **34**, 1771–1781. 86

WEST, A.J. & LOUTHAN, M.R. (1979). Dislocation transport and hydrogen embrittlement. *Metallurgical Transactions A*, **10**, 1675–1682. 83

XIUKUI, S., JIAN, X. & YIYI, L. (1989). Hydrogen permeation behaviour in austenitic stainless steels. *Materials Science and Engineering A*, **114**, 179–187. 65, 66, 68, 70

Chapter 5

Hydrogen Desorption in Multiphase Steel - TRIP

5.1   Introduction

Hydrogen thermal desorption in TRIP-assisted steels has been investigated by some researchers, however, most of studies have focused on the effects of plastic strain on hydrogen effusion (Pérez Escobar *et al.*, 2012; Ryu *et al.*, 2012). Since plastic strain causes the transformation of retained austenite into martensite, and at the same time increases dislocation density, the measured TDS curves are difficult to interpret unambiguously. In the work presented in this chapter, the effects of austenite fraction were studied by using a different intercritical annealing temperature. The numerical analysis method of single phase steel in chapter 3 and 4 is applied here to the measured data to assess the effects of austenite content.

5.2 Experimental and Results

5.2.1 Experimental

To compare the effects of austenite, samples with different austenite fractions were prepared using a Fe-0.11C-6.17Mn-0.98Al wt% TRIP-assisted steel. Fig. 5.1 shows the equilibrium phase fractions as a function of temperature calculated using *ThermoCalc* with the *TCFE6.2* database. Samples were intercritically annealed at 620, 660, 700 °C for 24 h using an infrared furnace. The heating and cooling rates were 400 and 200 °C h^{-1}, respectively.
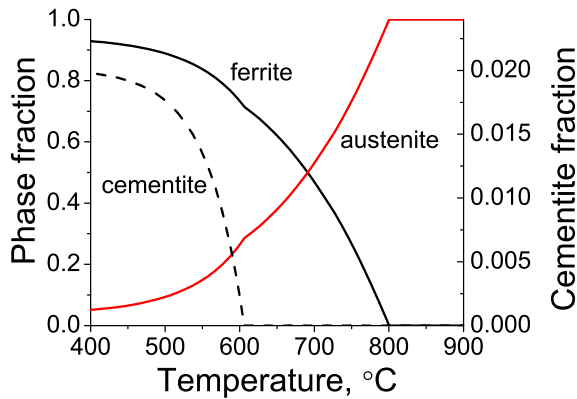
Figure 5.1: Calculated phase fractions of ferrite, austenite, and cementite using *ThermoClac* with *TCFE6.2*. Ferrite and austenite phases correspond to the left scale and cementite to the right scale.

The microstructure was observed using a field emission gun scanning electron microscope (FE-SEM) equipped with an electron back-scattered diffraction (EBSD) facility. In the latter case the specimens were electrochemically polished using a mixture of 10% perchloric acid and 90% acetic acid at 28 V. The retained austenite was determined using X-ray diffraction with CuK$_\alpha$ radiation; the samples in that case were mechanically polished and finally chemically polished in a 5% HF + H$_2$O$_2$ so-

lution. Integrated intensities of 100_α, 200_α, 211_α, and 111_γ, 200_γ, 220_γ reflections were used for the quantitative phase fraction measurement (Jatczak, 1980). Samples were also analyzed using transmission electron microscopy. Thin foil samples were produced by cutting slices from the specimens, thinning mechanically to $0.08\,\text{mm}$ by abrasion on SiC papers, and then twin-jet electro-polishing using a mixture of 5% perchloric acid and 95% acetic acid with a current of $60\,\text{mA}$.

For the TDS experiments, samples were cut into $50\,\text{mm}$ length, $12.5\,\text{mm}$ width and $1\,\text{mm}$ thickness. Each sample was polished with 800 grit sand papers, and charged electrochemically with hydrogen for $12\,\text{h}$ using 3% $NaCl + 0.3\%$ NH_4SCN solution with $1\,\text{A}\,\text{m}^{-2}$. TDS experiments started after $30\,\text{min}$ from the hydrogen charging. The results were analyzed at $3\,\text{min}$ intervals using helium as a carrier gas. The desorption rate was defined as the amount of hydrogen that evolves in $1\,\text{min}$. A standard mixture He + 10.2 volume ppm H_2 was used for calibrating the equipment. During the TDS experiment, the temperature is monitored via the equipment; therefore calibration experiments were conducted by attaching a thermocouple to the sample itself, and relating the directly measured temperature to that output by the TDS equipment.

5.2.2 Microstructure

Figs. 5.2 and 5.3 are representative microstructures and XRD results; the austenite fractions (V_γ) for the 620, 660 °C annealed samples are 0.26 $\pm$ 0.03, 0.36 $\pm$ 0.03, respectively. For the sample annealed at 700 °C the austenite peak was not observed from XRD, however, from EBSD analysis, V_γ is found to be 0.07. The grain sizes of ferrite and austenite are 1.98 $\pm$ 0.49 and 1.04 $\pm$ 0.31 μm for the case where $V_\gamma = 0.26$ and the grain sizes of ferrite and austenite are 1.43 $\pm$ 0.31 and 1.18 $\pm$ 0.28 μm for the sample with $V_\gamma = 0.36$. Twin boundaries were not counted and the values were obtained by lineal intercept method from *OIM* image analysis software. TEM image of the sample after holding at 620 °C for

93

24 h are shown in Fig. 5.4 and the obtained lattice parameters were 2.91 and 3.58 Å for ferrite and austenite, respectively.
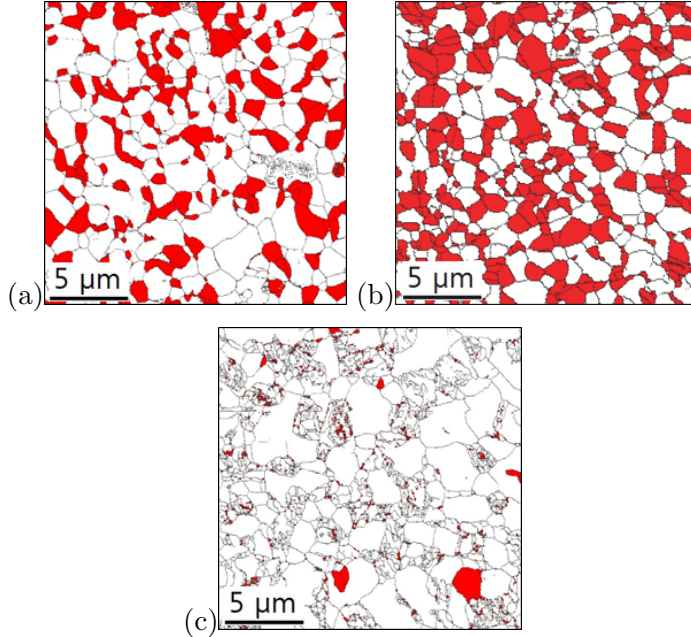
Figure 5.2: EBSD phase mappings of samples annealed at (a)620 °C, (b) 660 °C, (c) 700 °C in which ferrite and austenite is represented by white and red, respectively.

5.2.3 Hydrogen Desorption

The time for hydrogen charging was varied from 6 h to 96 h and the hydrogen amount as a function of charging time is shown in Fig. 5.5. When the sample contains no austenite, it is saturated before 24 h of charging. On the other hand, the samples with retained austenite saturated after 48 h of charging. The hydrogen concentrations were 3.4, 5.4 and 6.4 ppmw for the samples of which V_γ were 0, 0.26 and 0.36, respectively. However, note that those hydrogen values were measured after 45 min of room temperature aging after the hydrogen charging process finished.

Figure 5.3: XRD results for samples annealed at 620, 660, 700 °C for 24 h.
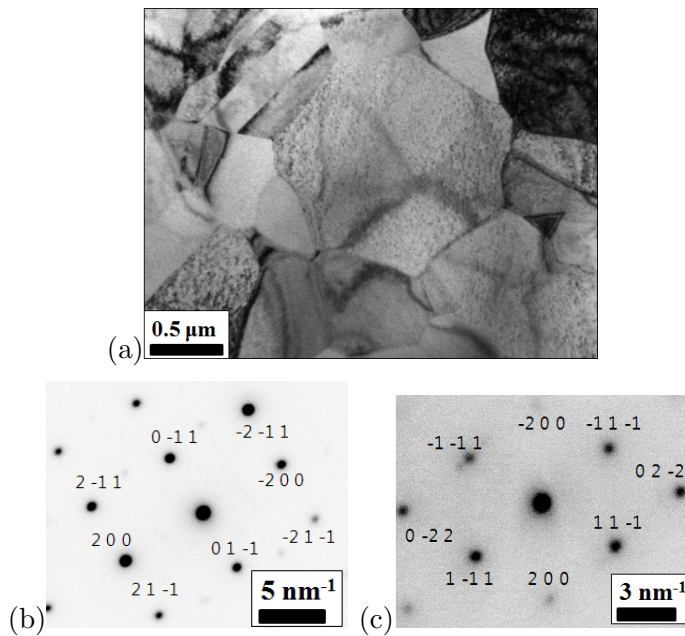
Figure 5.4: TEM image of the sample after holding at 620 °C for 24 h. (a) Bright field image, (b) diffraction pattern of [011] zone of ferrite and (c) diffraction pattern with [011] zone of austenite.

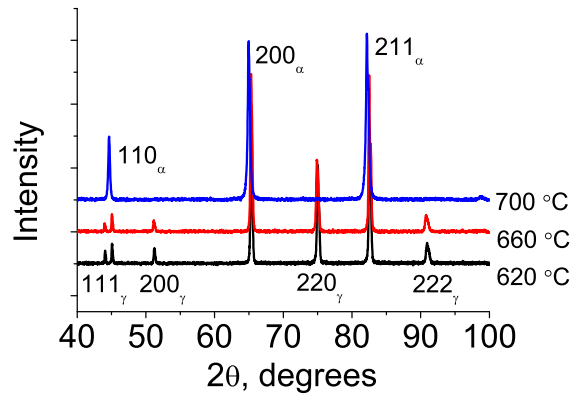The H amounts when austenite volume fraction is 0.0, 0.26 and 0.36 are 3.5, 5.8 and 6.6 ppmw, respectively when they were measured after 30 min of room temperature aging after hydrogen charging process finished.
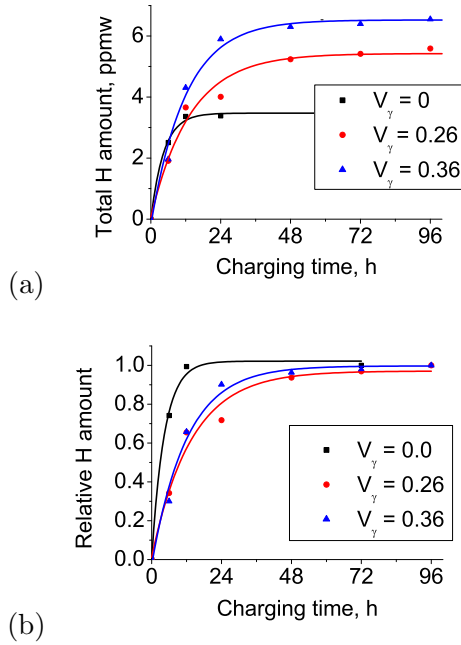
Figure 5.5: (a) Total hydrogen content as a function of charging time and (b) Relative hydrogen content as a function of charging time. Measured hydrogen contents were divided by their saturated values.

The TDS curves of samples of 6, 24, and 72 h charging time are shown in Fig. 5.6. For all the cases, the heating rate was $100\,^{\circ}\mathrm{C}\,\mathrm{h}^{-1}$. After 6 h of charging, the desorption peak from the sample without austenite is higher and the peak temperature is lower than those of the samples with austenite. As charging time increases, the desorption peaks from the sample with austenite become higher while the change in the sample without austenite is small. The results after 72 h of charging could be regarded as those from saturated samples. Only one peak was observed up

Figure 5.6: Measured TDS curves with different austenite fractions after (a) 6 h, (b) 24 h and (c) 72 h of charging.

to 300 °C and the area enclosed by the peak increases with the austenite fraction.

To summarize, the effects of austenite are the increase of diffusible hydrogen amount and sample saturation time. In this study, a model for hydrogen desorption in multiphase steel is suggested and by using the model, the experimental results are analyzed.

5.3 Numerical Analysis

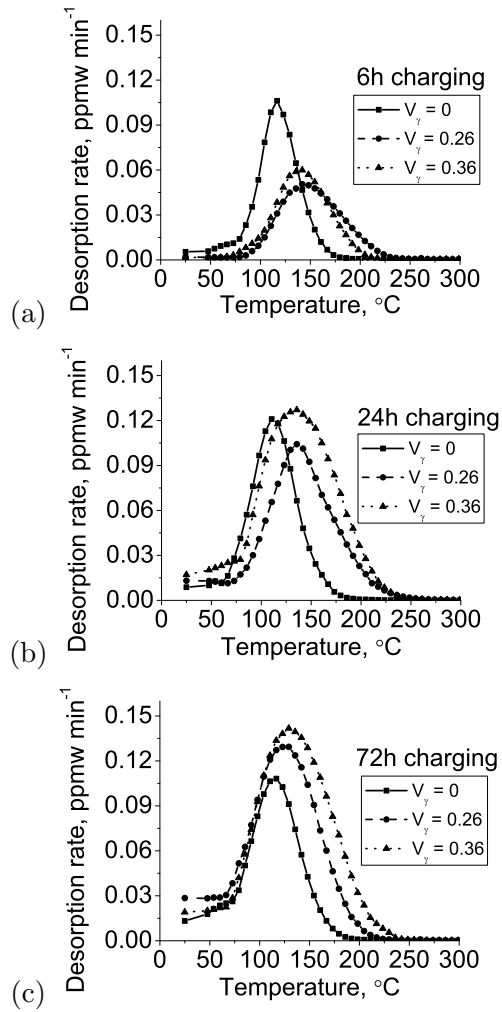The TDS results were analyzed assuming austenite as a trap. If the sample is assumed to be a semi-infinite bar and its initial concentration is uniform as C_0, and its surface concentration is zero, then the following holds.

$$C(x) = C_0 \operatorname{erf}\left(\frac{x}{2\sqrt{Dt}}\right) \tag{5.1}$$

When the diffusion distance x is defined such that $C(x) = \frac{C_0}{2}$, then

$$\operatorname{erf}\left(\frac{x}{2\sqrt{Dt}}\right) = 1/2 \tag{5.2}$$

Since $\operatorname{erf}(0.5) \sim 0.5$, the following holds.

$$x = \sqrt{Dt} \tag{5.3}$$

The diffusion distance of hydrogen in austenite for 3 min can be calculated and the results are shown in Fig. 5.7. The diffusivity of hydrogen in austenite was from the literature (Xiukui *et al.*, 1989).

Given that the diffusion distance for 3 min is much longer than the austenite size $\sim 1\,\mu\text{m}$ at temperatures above 120 °C where the desorption peak appears, diffusion within austenite was ignored and austenite was treated as a trap. The trapping by dislocations is not considered given that these are intercritically annealed samples, but trapping by grain boundaries and austenite was accounted for.
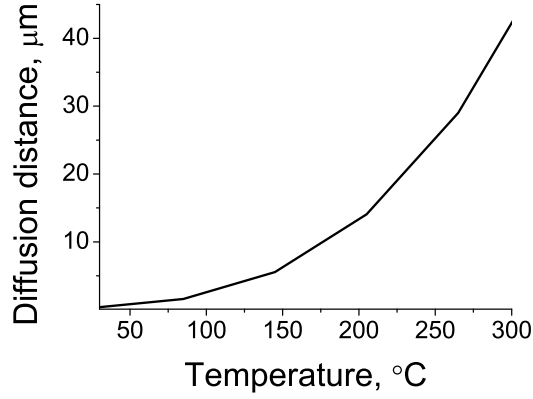
Figure 5.7: The diffusion distance of hydrogen in austenite for $3\,\mathrm{min}$ as a function of temperature.

The transfer of atom from the austenite trap to the ferrite can only occur at the α/γ interface. Since diffusion within the austenite is not rate limiting, the problem was treated by assuming that all of the hydrogen that is in the austenite is in fact available at the interface, to be released into the ferrite at a rate determined by temperature and the binding energy, and consistent with local equilibrium.

The α/γ interfacial area per unit volume S_V can be obtained from $2/\bar{L}$ where $\bar{L}$ is the average grain size from the lineal intercept method. From OIM image analysis software, the fractions of α-γ boundary area to the total boundary area are 0.31 and 0.38 when V_γ are 0.26 and 0.36, respectively. Then the density for austenite trapping can be obtained as

$$N_t = A\frac{S_V^\gamma}{r^2} \tag{5.4}$$

where S_V^γ is the α/γ boundary area per unit volume and r is the effective size of an hydrogen atom. The actual size of an hydrogen atom is $1.06\,\text{Å}$ however, r was used as twice of its actual size by considering the repulsion between near neighbour hydrogen pairs (Minot & Demangeat, 1985). In

99

order to accommodate the hydrogen that is related in inside the austenite, the trap density N_t was exaggerated by constant A. In this study, A was used as 4.1 so that it can gives the best fit with the measured data. The method therefore ensures that the total amount of hydrogen released in the TDA is about the same as in the modelled curve. There is therefore one fitting parameter (A/r^2), obtained from the V_γ=0.36 sample, and used to predict the results for V_γ=0.26.

The trap density of grain boundaries was assumed to be $1.6 \times 10^{24}\,\mathrm{m^{-3}}$ which was obtained in chapter 3. and the obtained total trap densities are 4.55×10^{25} and $4.96 \times 10^{25}\,\mathrm{m^{-3}}$ when V_γ are 0.26 and 0.36, respectively. The measured data and predicted results are shown in Fig. 5.8 for the parameters in Table 5.1. The results were produced with one trap binding energy because trapping is allowed only at the α/γ boundaries.
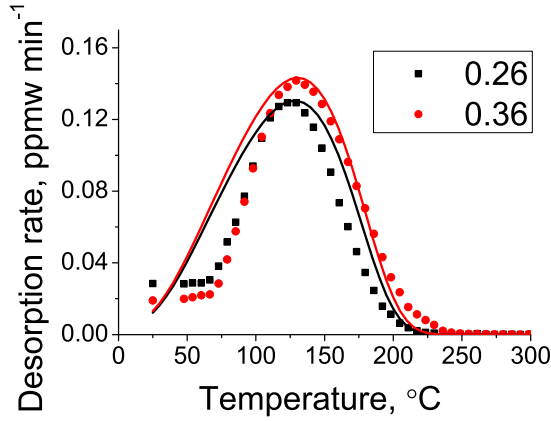

Figure 5.8: Measured TDS data and predicted results with different austenite fractions.

5.3.1 Other Approaches

Apart from artificially increasing the trap density at the α/γ interfaces in order to accommodate the hydrogen that is in austenite, other meth-

Table 5.1: The binding energies ($\mathrm{kJ\,mol^{-1}}$) and trap densities ($10^{25}\,\mathrm{m^{-3}}$) for the samples with different austenite fraction.

	$V_\gamma = 0.26$	$V_\gamma = 0.36$
binding energy	50	50
trap density	4.55	4.96

ods for compensating the hydrogen inside austenite were tried with the parameters in Table 5.1. First, the hydrogen concentration in α/γ interfaces was forced to be larger than its equilibrium value so that it can reflect the total hydrogen inside the austenite. However, in this case, the extra hydrogen effuses immediately, due to the local equilibrium assumption, resulting in exactly the same results as those in Fig. 5.8. Second, a hydrogen reservoir was assumed so that the reduction of hydrogen in austenite surface during heating was replenished from the reservoir immediately. The amount in the reservoir was calculated from the solution energy difference ΔH_s between ferrite and austenite. The values were obtained from Song *et al.* (2013).

$$\frac{C_\gamma}{C_\alpha} = \exp\left(\frac{\Delta H_s}{RT}\right) \tag{5.5}$$

In this case, the extra peak about $40\,°\mathrm{C}$ was observed as shown in Fig. 5.9. However, the results are closely related with the extent of the reservoir and require further study.

5.3.2 Saturation of Charging

In addition, note that all these results were predicted from the saturated samples. If austenite simply acts as a trap, the difference in TDS curves of samples with and without austenite is explained by the trap density increase due to the existence of austenite. The total hydrogen content as a function of charging time was calculated with the samples with pa-
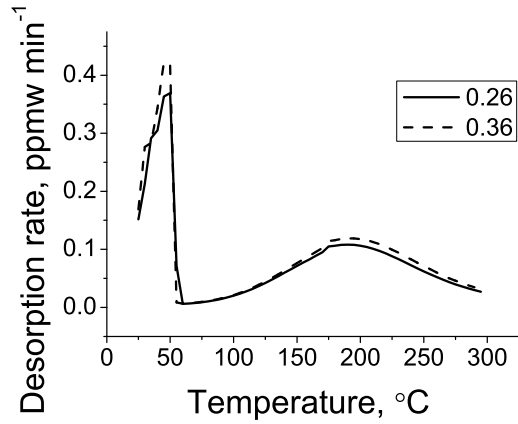
Figure 5.9: Predicted results with different austenite fractions with a reservoir.
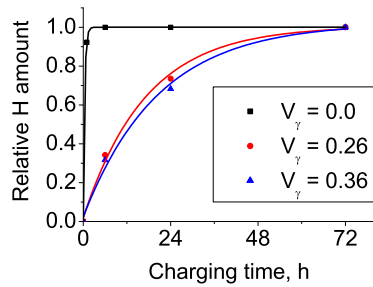

Figure 5.10: Relative hydrogen content as a function of charging time from simulation. Those hydrogen contents were divided by their saturated value.

rameters in Table 5.1. Even though the surface concentration has little effect on the TDS curves of saturated samples as shown in chapter 3, it affects the sample saturation time significantly by adjusting the flux from surface. The surface concentration was set at 0.001 ppmw so that the hydrogen content curve in Fig. 5.5b with austenite can be reproduced. Note the reported hydrogen solubility in pure iron with 1 atm H_2 is 0.0001 (San-Martin & Manchester, 1990) and that in low-alloy steel is 0.009 ppmw (Hickel *et al.*, 2014) when it is in equilibrium with 1 atm of H_2. For the sample without austenite, only the trapping by grain boundaries was considered. Predicted results are shown in Fig. 5.10. In future work, it would be useful to consider diffusion within austenite.

References

Hickel, T., Nazarov, R., McEniry, E., Leyson, G., Grabowski, B. & Neugebauer, J. (2014). Ab initio based understanding of the segregation and diffusion mechanisms of hydrogen in steels. *JOM*, **66**, 1399–1405. 103

Jatczak, C.F. (1980). Retained austenite and its measurement by X-ray diffraction. Tech. rep., SAE Technical Paper. 93

Minot, C. & Demangeat, C. (1985). Binding energy of a pair of hydrogen atoms in α-iron. *Physics Letters A*, **108**, 285–288. 99

Pérez Escobar, D., Depover, T., Duprez, L., Verbeken, K. & Verhaege, M. (2012). Combined thermal desorption spectroscopy, differential scanning calorimetry, scanning electron microscopy and X-ray diffraction study of hydrogen trapping in cold deformed trip steel. *Acta Materialia*, **60**, 2593–2605. 91

RYU, J.H., CHUN, Y.S., LEE, C.S., BHADESHIA, H. & SUH, D.W. (2012). Effect of deformation on hydrogen trapping and effusion in trip-assisted steel. *Acta Materialia*, **60**, 4085–4092. 91

SAN-MARTIN, A. & MANCHESTER, F. (1990). The Fe-H (iron-hydrogen) system. *Bulletin of Alloy Phase Diagrams*, **11**, 173–184. 103

SONG, E.J., BHADESHIA, H. & SUH, D.W. (2013). Effect of hydrogen on the surface energy of ferrite and austenite. *Corrosion Science*, **77**, 379–384. 101

XIUKUI, S., JIAN, X. & YIYI, L. (1989). Hydrogen permeation behaviour in austenitic stainless steels. *Materials Science and Engineering A*, **114**, 179–187. 98

Chapter 6

Conclusions

A numerical method that incorporates both diffusion and detrapping process has been implemented to account for the practical experiments. The detrapping process was simulated using two different models; first model assumes local equilibrium between trapped and free hydrogen and the other model considers only kinetics of detrapping without local equilibrium assumption. However, the results of the local equilibrium model and kinetic models were found to be consistent *i.e.*, an equilibrium distribution of hydrogen is maintained at all temperatures. It was also found that the desorption peak is separated in the samples with multiple traps, if the difference in binding energies are large enough.

This model was tested against new experimental data and the influence of plastic strain on hydrogen desorption in ferrite was assessed. The measured data were successfully reproduced from this model when the binding energy of dislocations were set at $53\,\mathrm{kJ\,mol^{-1}}$ and the trap densities were calculated assuming it to be proportional to the dislocation density. In addition, the effects of carbon segregation on hydrogen desorption in ferrite was investigated using bake hardening steel. It was found that carbon segregation has no effect on the binding energy of dislocations but it decreased the trap density.

This model was able to be applied in unsaturated austenite samples and the effects of aluminum addition were assessed. From the first-principles calculation, the binding energy of aluminum in austenite was obtained to be $6\,\mathrm{kJ\,mol^{-1}}$ and the trap density was calculated by considering the concentration of aluminum. From the simulation with those parameters, the desorption peak height increased when aluminum is added but no significant change in the peak temperature was found. In addition, the effects of grain size were analyzed with reported data. The binding energy of grain boundaries in austenite was evaluated to be $15\,\mathrm{kJ\,mol^{-1}}$ which indicates the grain boundaries in austenite are much less potent than those in ferrite.

The effects of austenite in hydrogen desorption in TRIP-assisted steel were studied. From TDS experiment, it was found that the diffusible hydrogen amount and sample saturation time increased with the austenite fraction and only one peak was observed upto $300\,^{\circ}\mathrm{C}$. The results were also analyzed with the numerical model. Detrapping of hydrogen that is in austenite is allowed at the α/γ boundaries considering transport of hydrogen atom from austenite to ferrite can happen only at boundaries. Instead the trap density N_t was exaggerated in order to accommodate the hydrogen that is related in inside the austenite.